Journal of Computational Physics ••• (••••) ••••••

Contents lists available at ScienceDirect

Journal of Computational Physics

journal homepage: www.elsevier.com/locate/jcp

Hybrid LBM-FVM solver for two-phase flow simulation

Yihui Ma [a], Xiaoyu Xiao [a], Wei Li [b], Mathieu Desbrun [c], Xiaopei Liu [a,*]

[a] SIST, Shanghaitech University, China
[b] Inria, IP Paris, France
[c] Inria/Ecole Polytechnique, IP Paris, France

ARTICLE INFO

Keywords:
Two-phase flow simulation
Lattice Boltzmann method
Finite-volume method

ABSTRACT

In this paper, we introduce a hybrid LBM-FVM solver for two-phase fluid flow simulations in which interface dynamics is modeled by a conservative phase-field equation. Integrating fluid equations over time is achieved through a velocity-based lattice Boltzmann solver which is improved by a central-moment multiple-relaxation-time collision model to reach higher accuracy. For interface evolution, we propose a finite-volume-based numerical treatment for the integration of the phase-field equation: we show that the second-order isotropic centered stencils for diffusive and separation fluxes combined with the WENO-5 stencils for advective fluxes achieve similar and sometimes even higher accuracy than the state-of-the-art double-distribution-function LBM methods as well as the DUGKS-based method, while requiring less computations and a smaller amount of memory. Benchmark tests (such as the 2D diagonal translation of a circular interface), along with quantitative evaluations on more complex tests (such as the rising bubble and Rayleigh-Taylor instability simulations) allowing comparisons with prior numerical methods and/or experimental data, are presented to validate the advantage of our hybrid solver. Moreover, 3D simulations (including a dam break simulation) are also compared to the time-lapse photography of physical experiments in order to allow for more qualitative evaluations.

1. Introduction

Two-phase flows feature prominently in many natural phenomena, as well as in a majority of processing technologies where handling interface flow becomes important. In the literature, the interface between two immiscible fluids is typically modeled using either sharp interface methods which keep track of a zero-thickness interface over time, or with diffuse interface methods which assume a finite thickness of the interface instead, making interface tracking easier to achieve [1,2]. A popular approach to two-phase flow simulation with diffuse interface modeling is to use a Cahn–Hilliard [3] or Allen–Cahn [4] equation for the evolution of a *phase-field function* taking the role of an order parameter [5–7]. Coupled with the Navier–Stokes (N-S) equations for fluid dynamics, the whole set of partial differential equations is then evolved by integrating in time typically using the conservative finite-volume method (FVM) [8].

In contrast to traditional FVM solvers, the lattice Boltzmann method (LBM) [9] has emerged as a promising alternative to efficiently solve fluid equations for both single- and two-phase flows [10]. LBM is constructed from the kinetic theory describing the fluid flow by a set of discrete distribution functions $f_i(\mathbf{x}, t)$, which are then evolved over time by repeated streaming and collision processes. While streaming is relatively straightforward as it simply transfers distribution functions to neighboring nodes, collision

* Corresponding author.
E-mail address: liuxp@shanghaitech.edu.cn (X. Liu).

https://doi.org/10.1016/j.jcp.2024.112920
Received 2 May 2022; Received in revised form 6 March 2024; Accepted 6 March 2024

modeling is key to an accurate and stable solution for LBM. In the past decades, different collision models have been proposed to improve numerical stability: from the lattice Bhatnagar-Gross-Krook (LBGK) model [9] and the raw-moment multiple-relaxation-time (RM-MRT) model [11] which unfortunately failed to satisfy Galilean invariance, to a series of central-moment multiple-relaxation-time (CM-MRT) models [12–15] as well as the regularized collision model [16], and more recently, to the cumulant model [17–19], the spurious modes for high Reynolds number flows using early collision models due to influence of numerical truncation have been significantly reduced, thus improving stability and accuracy for simulation in a large range of Reynolds numbers. Moreover, the local nature of the LBM updates and of the different types of bounce-back schemes [20,21] to deal with complex boundaries allows for massively-parallel implementation [22], especially on current GPUs [23].

While single-phase flows with turbulence and with fluid-structure interaction have already been extensively studied in academia as well as in industry [24–26], the simulation of two-phase flows has gradually gained increased attention over the past decade. Several formulations (based on color gradient [27–31], pseudo-potential [32–34], free energy [35–40], as well as phase field [41, 42] models to name a few) have been proposed, among which the phase-field approach is arguably the most popular one due to strong theoretical foundations; by now, it has been successfully developed within the lattice Boltzmann (LB) framework by several authors [43,44,42,45–47].

However, most available phase-field lattice Boltzmann solvers rely on double distribution functions (DDF) where a second set of distribution functions is used to solve the phase-field equation, thus doubling the memory cost and preventing higher resolution simulation on a single GPU. Although in-place streaming (such as [48]) can be used to reduce the memory by half, we argue in this paper that there is still room for further reduction of memory by solving the phase-field equation based on an FVM-based discretization. Together with a velocity-based collision model improved by central-moment formulation, this new approach results in a hybrid LBM-FVM solver that not only enables higher grid resolutions given a fixed amount of memory for simulation, but also can reach similar and sometimes even higher accuracy than existing methods. In that respect, our approach improves upon similar hybrid methods [49,50] by respectively enforcing a conservative evolution of the phase-field function and leveraging higher-order approximation models to allow for more accurate and more efficient two-phase flow simulations with high Reynolds numbers and large density ratios.

Contributions. In this paper, we propose a novel hybrid solver for two-phase flow simulations where the interface evolution is modeled by the Allen-Cahn equation [51]. To enable better incompressibility and thus higher accuracy especially for flows with a high density ratio between fluids, a velocity-based lattice Boltzmann formulation is employed to solve for the fluid flow, and a new finite-volume solver is formulated and applied to the phase-field equation where higher-order reconstructions are used for fluxes across cell faces as compared to [50], resulting in improved stability and accuracy. Importantly, our hybrid approach systematically requires a smaller memory footprint than the DDF-LBM solvers [52,19] or the DUGKS solver [53] for a similar accuracy on benchmark tests, whether in-place streaming is used or not. We implemented our hybrid solver on a single GPU, for both 2D and 3D simulations. To quantify the accuracy of our solver for interface evolution, we tested our FVM-based phase-field solver on the diagonal translation of a circular interface, the Zalesak disk, as well as a circular interface in a shear flow, and compare our numerical results to the state-of-the-art methods. We also tested our coupled two-phase flow hybrid solver on the more challenging examples of a bubble rising and the Rayleigh-Taylor instability to quantitatively evaluate closeness to the experimental measurements, with accuracy exceeding existing numerical results in some of these tests. We further show 3D simulations that we compare to time-lapse photographs of a real experiment to evaluate qualitatively our solver for two-phase flows in more complex setups. Finally, performance of our solver is analyzed and discussed to highlight that the reduction in memory usage also enhances computational efficiency.

Outline. The remainder of this paper is organized as follows. Sec. 2 reviews the phase-field equation and the lattice Boltzmann solver for fluid flows based on which we propose our contributions: we introduce in Sec. 2.1 the formulation of the conservative phase-field equation for interface tracking along with the incompressible Navier-Stokes (N-S) equations describing the fluid dynamics; we then discuss our FVM-based discretization of the conservative phase-field equation in Sec. 2.2; in Sec. 2.3, we briefly describe the velocity-based LBM approach which we employ and modify with a CM-MRT formulation for fluid flow equations, as well as its coupling with the phase-field solver. We then present in Sec. 3 the numerical evaluations of our approach by benchmark tests and validations using several well-known test examples, followed by further discussions of our method. Sec. 4 concludes with a summary of our paper.

2. Methodology

We begin with a brief introduction to the phase-field theory for two-phase flow simulations based on Allen-Cahn equations [54], before describing our new LBM-FVM-based hybrid numerical method for solving such a system.

2.1. Conservative phase-field equation and governing equations for hydrodynamics

Suppose we want to simulate two immiscible and incompressible Newtonian fluids with density ρ_H and ρ_L and viscosity ν_H and ν_L, respectively, where the subscripts H and L are used to differentiate the high-density fluid from the low-density one in our exposition. In order to identify the regions occupied by the two fluids, the diffuse interface model [55,56] introduces a time-varying phase-field function $\phi(x,t)$ as an order parameter, where:

$$\phi(x,t) = \begin{cases} \phi_H, & \text{inside high-density fluid,} \\ \phi_L, & \text{inside low-density fluid,} \end{cases} \tag{1}$$

with a smooth, thin transition layer of thickness ξ between the two fluids. For notational simplicity and without loss of generality, we will use $\phi_H = 1$ and $\phi_L = 0$ in the remainder of this paper. The interface may thus be defined as the iso-surface where the phase-field function takes the value of ½, and the phase-field equation allows to substitute boundary conditions on the sharp interface by a partial differential equation for the evolution of the phase-field function to reproduce the correct interfacial dynamics.

Phase-field model. A typical phase-field model [6,57,58] is constructed using a simple, explicit expression for the free energy W of the system, which involves a Ginzburg-Landau double-well potential F describing the free energy density of the bulk of each phase and an interfacial Dirichlet energy, resulting in an integral over the physical domain Ω occupied by the two-phase flow system [57]:

$$W(\phi, \nabla\phi) = \int_{\Omega} [F(\phi) + \frac{\kappa}{2}|\nabla\phi|^2], \tag{2}$$

where $F(\phi) = \beta\phi^2(\phi-1)^2$, with β and κ being positive constants. For a given interfacial thickness ξ and a surface tension σ, these values of the free energy are respectively defined as [59]

$$\xi = \sqrt{8\kappa/\beta}, \qquad \sigma = \frac{1}{6}\sqrt{2\kappa\beta}, \tag{3}$$

or equivalently, $\beta = 12\sigma/\xi$ and $\kappa = 3\sigma\xi/2$.

Interface profile. Since the chemical potential μ is the rate of change of free energy, the assumption that the diffuse interface is at equilibrium when its chemical potential is null leads to:

$$\mu = \frac{\partial W}{\partial \phi} = 4\beta\phi(\phi-1)(\phi-\tfrac{1}{2}) - \kappa\nabla^2\phi = 0. \tag{4}$$

One can verify that in the 1D case, the interface profile at equilibrium satisfies:

$$\phi(x) = \frac{1}{2}\left[1 + \tanh(2d(x)/\xi)\right], \tag{5}$$

where $d(x)$ is the signed distance of position x to the interface defined as $\phi(x) = 1/2$.

Equation for interface motion. A conservative form of the interface evolution can be expressed via a modified Allen-Cahn equation [54,43,44] as:

$$\frac{\partial\phi}{\partial t} + \nabla\cdot(\underbrace{\phi\mathbf{u}}_{\mathbf{J}_1}) = \nabla\cdot\underbrace{\left[M\left(\nabla\phi - \frac{4}{\xi}\phi(1-\phi)\mathbf{n}\right)\right]}_{\mathbf{J}_2}, \tag{6}$$

where $\mathbf{n}$ represents the unit vector field aligned with the gradient of the phase-field function, i.e.,

$$\mathbf{n} = \frac{\nabla\phi}{\|\nabla\phi\|}. \tag{7}$$

The mobility parameter M controls the degree of interface splitting, i.e., a small M implies a greater ease for the interface to split since less diffusion is introduced. Note that $\mathbf{J}_1$ is an advective flux density making the phase-field function advected by the fluid velocity field $\mathbf{u}$, while $\mathbf{J}_2$ is the sum of a diffusive flux density and of a separation flux density imposing a predefined interface profile in 3D of the form:

$$\phi(\mathbf{x}) = \frac{1}{2}\left[1 + \tanh\left(2d(\mathbf{x})/\xi\right)\right], \tag{8}$$

where $d(\mathbf{x}) = \pm|\mathbf{x} - \bar{\mathbf{x}}|$ is the signed distance of point $\mathbf{x}$ to its orthogonal projection $\bar{\mathbf{x}}$ on the interface (i.e., $\phi(\bar{\mathbf{x}}) = 1/2$), with the convention that positive distances are in the high density phase and negative distances are in the low density phase.

Equation for fluid flow. In our two-phase fluid flow context, the fluid flow is governed by the incompressible Navier-Stokes equations [60], i.e.,

$$\begin{cases} \nabla\cdot\mathbf{u} = 0, \\ \dfrac{\partial\rho}{\partial t} + \nabla\cdot(\rho\mathbf{u}) = 0, \\ \dfrac{\partial(\rho\mathbf{u})}{\partial t} + \nabla\cdot(\rho\mathbf{u}\otimes\mathbf{u}) = -\nabla p + \rho\nu\nabla^2\mathbf{u} + \mathbf{F}_s + \mathbf{F}_b. \end{cases} \tag{9}$$

Here, p is the hydrodynamic pressure, ν is the kinematic viscosity, $\mathbf{F}_b = \rho\mathbf{g}$ is the body force (where $\mathbf{g}$ is the gravitational acceleration), and $\mathbf{F}_s$ is the surface tension force which takes the form $\mathbf{F}_s = \mu\nabla\phi$ in our phase-field model. The fluid density ρ is defined through a linear relationship with the phase-field function [52] as

$$\rho(\phi) = (1-\phi)\rho_L + \phi\rho_H. \tag{10}$$

The kinematic viscosity in the diffuse-interface method takes, instead, an inverse linear form [61] expressed as:

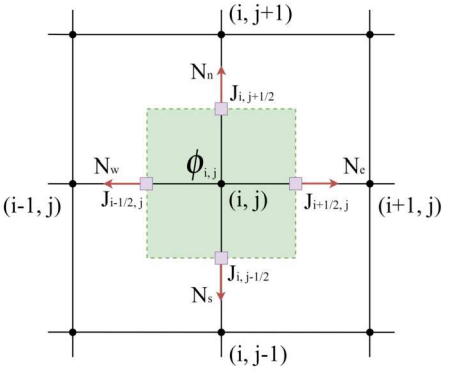

Fig. 1. Schematic diagram of our finite-volume approach to integrate the phase-field equation on a uniform grid. The values **J** on the sides of the green box denote fluxes of the fluid flow moving in and out, which are used to update the phase-field value at node (i, j). (For interpretation of the colors in the figure(s), the reader is referred to the web version of this article.)

$$\frac{1}{\nu} = (1-\phi)\frac{1}{\nu_L} + \phi\frac{1}{\nu_H}. \tag{11}$$

For turbulent fluids, we employ the wall-adapted large-eddy (WALE) model [62] to predict an eddy viscosity ν' at each grid node as a mean subgrid effect that is added to the kinematic viscosity ν for simulation through $\nu \leftarrow \nu + \nu'$, similar to [63].

2.2. Finite-volume solver for phase-field equation

In order to integrate the modified Allen-Cahn equation (Eq. (6)) for the phase-field evolution in time, we propose to use a new finite-volume-based formulation with a proper flux reconstruction which is intrinsically conservative. Using $\mathbf{J} = \mathbf{J}_2 - \mathbf{J}_1$ for conciseness, Eq. (6) once integrated over a small control volume V yields [50]:

$$\int_V \frac{\partial \phi}{\partial t}\, dV = \int_V \nabla \cdot \mathbf{J}\, dV = \oint_S \mathbf{J} \cdot \mathbf{N}\, ds, \tag{12}$$

where we applied for the last equality the divergence theorem on a fluid domain V and its boundary $S = \partial V$, with $\mathbf{N}$ denoting the unit normal vector of S facing outwards.

Since we will simulate the fluid motion through an LBM-based method relying on a (primal) regular grid with the distribution functions sampled on grid nodes, we use a dual grid (forming also a regular grid) for our integration of the phase-field equation as illustrated in Fig. 1 to offer a compatible treatment of the phase-field function and velocity field: by ensuring that all the dual cell values are updated using fluxes of **J** through dual faces, we leverage the conservative nature of Eq. (12) to update in time the phase-field function on the nodes of the primal grid, i.e., collocated with the nodes of the distribution functions of the fluid. The discretization of Eq. (12) (in 2D only for simplicity) can thus be expressed on the dual cell $V_{i,j}$ associated with the primal node (i, j) as:

$$\frac{\phi_{i,j}^{t+1} - \phi_{i,j}^{t}}{\Delta t} = [\ \mathbf{J}_{i+½,j} \cdot \mathbf{N}_e + \mathbf{J}_{i-½,j} \cdot \mathbf{N}_w + \mathbf{J}_{i,j+½} \cdot \mathbf{N}_n + \mathbf{J}_{i,j-½} \cdot \mathbf{N}_s\ ]\, \Delta x, \tag{13}$$

where $\phi_{i,j}^{t}$ is the phase-field function value in volume $V_{i,j}$ at time t; Δt and Δx are the time step and spatial cell size, while the values with non-integer indices indicate fluxes, e.g., $\mathbf{J}_{i+½,j}$ is the flux of **J** through the dual face between $V_{i,j}$ and $V_{i+1,j}$, consistently oriented towards the increasing indices (see Fig. 1).

Computing fluxes. There are multiple approaches to compute the fluxes, and we settled on a relatively simple approach for our simulation which is efficient, yet accurate. The value $\mathbf{J}_{i+½,j}$ for instance, corresponding to the flux of $\mathbf{J} = \mathbf{J}_2 - \mathbf{J}_1$ through the vertical wall between cell $V_{i,j}$ and $V_{i+1,j}$, is computed as the difference between flux $\mathbf{J}_{1(i+½,j)}$ and flux $\mathbf{J}_{2(i+½,j)}$. The latter is straightforwardly evaluated as follows:

$$\mathbf{J}_{2(i+½,j)} = M\left[\nabla\phi_{i+½,j} + \frac{4}{\xi}\left(\phi_{i+½,j}\left(1-\phi_{i+½,j}\right)\mathbf{n}_{i+½,j}\right)\right], \tag{14}$$

where the x-aligned phase-field gradient $\nabla\phi_{i+½,j}$ is computed to the second-order accuracy as the centered evaluation $(\phi_{i+1,j} - \phi_{i,j})/\Delta x$. The phase-field function values at half indices are averages of their nearby nodes, i.e.,

$$\phi_{i+½,j} = \left(\phi_{i,j} + \phi_{i+1,j}\right)/2, \tag{15}$$

and the normalized phase-field gradients evaluated at half indices are also obtained through averaging between two adjacent nodes:

$$\mathbf{n}_{i+½,j} = \left(\mathbf{n}_{i+1,j} + \mathbf{n}_{i,j}\right)/2. \tag{16}$$

Finally, we evaluate the phase-field gradients at grid nodes through a second-order weighted isotropic finite-difference scheme [64], which coincides with the isotropic phase-field gradient evaluation used in [52], i.e., for w_k being the quadrature weights and $\mathbf{c}_k$ the discrete velocities used in LBM (see App. A.1), we compute

$$(\nabla\phi)_{i,j} = 3\sum_k w_k\,\mathbf{c}_k\,\frac{\phi_{i+(\mathbf{c}_k)_x,j+(\mathbf{c}_k)_y} - \phi_{i,j}}{\Delta x}. \tag{17}$$

For $\mathbf{J}_1$, corresponding to the convective term, we use an upwind high-order WENO-5 treatment for this hyperbolic component of the evolution equation [65]. For completeness, we briefly review this high-order evaluation procedure in 2D. The discrete form of the integral mentioned in Eq. (12) at a grid node (i,j) is

$$\begin{aligned}\oint_S \mathbf{J}_1\cdot\mathbf{N}\,dS \equiv [\ &\phi_{i+½,j}\mathbf{u}_{i+½,j}\cdot\mathbf{N}_e + \phi_{i-½,j}\mathbf{u}_{i-½,j}\cdot\mathbf{N}_w \\ &+ \phi_{i,j+½}\mathbf{u}_{i,j+½}\cdot\mathbf{N}_n + \phi_{i,j-½}\mathbf{u}_{i,j-½}\cdot\mathbf{N}_s\ ]\,\Delta x \\ &= [\ \phi_{i+½,j}u_{x,(i+½,j)} - \phi_{i-½,j}u_{x,(i-½,j)} \\ &+ \phi_{i,j+½}u_{y,(i,j+½)} - \phi_{i,j-½}u_{y,(i,j-½)}\ ]\,\Delta x.\end{aligned} \tag{18}$$

The velocity on the face between $V_{i,j}$ and $V_{i+1,j}$ is computed from the average of two adjacent nodes as:

$$\mathbf{u}_{i+½,j} = (\mathbf{u}_{i,j} + \mathbf{u}_{i+1,j})/2. \tag{19}$$

As an upwind scheme, the surrounding five stencil points for the calculation of $\phi_{i+½,j}$ are chosen as

$$\mathbf{stencil} = \begin{cases} \{(i-2,j),\ (i-1,j),\ (i,j),\ (i+1,j),\ (i+2,j)\} & \text{if } \mathbf{u}_x \geq 0 \\ \{(i-1,j),\ (i,j),\ (i+1,j),\ (i+2,j),\ (i+3,j)\} & \text{if } \mathbf{u}_x < 0 \end{cases}. \tag{20}$$

That is, based on the sign of the flux determined by the resulting velocity calculated from Eq. (19), we evaluate the phase-field function values on the dual face using three distinct finite-difference stencils: assuming for instance that the flux is positive ($\mathbf{u}_x \geq 0$), we evaluate:

$$\begin{aligned}\phi^{[1]}_{i+½,j} &= \frac{1}{3}\phi_{i-2,j} - \frac{7}{6}\phi_{i-1,j} + \frac{11}{6}\phi_{i,j}, \\ \phi^{[2]}_{i+½,j} &= -\frac{1}{6}\phi_{i-1,j} + \frac{5}{6}\phi_{i,j} + \frac{1}{3}\phi_{i+1,j}, \\ \phi^{[3]}_{i+½,j} &= \frac{1}{3}\phi_{i,j} + \frac{5}{6}\phi_{i+1,j} - \frac{1}{6}\phi_{i+2,j}.\end{aligned}$$

Similarly for a negative flux based on Eq. (20). Smoothness indicators $\{\beta_i\}_{i=1..3}$ are evaluated on each of these stencils' support through [66]:

$$\begin{aligned}\beta_1 &= \frac{13}{12}\left(\phi_{i-2,j} - 2\phi_{i-1,j} + \phi_{i,j}\right)^2 + \frac{1}{4}\left(\phi_{i-2,j} - 4\phi_{i-1,j} + 3\phi_{i,j}\right)^2, \\ \beta_2 &= \frac{13}{12}\left(\phi_{i-1,j} - 2\phi_{i,j} + \phi_{i+1,j}\right)^2 + \frac{1}{4}\left(\phi_{i-1,j} - \phi_{i+1,j}\right)^2, \\ \beta_3 &= \frac{13}{12}\left(\phi_{i,j} - 2\phi_{i+1,j} + \phi_{i+2,j}\right)^2 + \frac{1}{4}\left(3\phi_{i,j} - 4\phi_{i+1,j} + \phi_{i+2,j}\right)^2.\end{aligned}$$

A 5th-order accurate reconstruction of the phase-field function value $\phi_{i+½,j}$ can then be obtained through a linear combination of the three third-order finite-difference estimates computed above as:

$$\phi_{i+\frac{1}{2},j} = \omega_1\phi^{[1]}_{i+\frac{1}{2},j} + \omega_2\phi^{[2]}_{i+\frac{1}{2},j} + \omega_3\phi^{[3]}_{i+\frac{1}{2},j}, \tag{21}$$

where the three positive coefficients ω_j are evaluated as:

$$\omega_j = \frac{\tilde{\omega}_j}{\tilde{\omega}_1 + \tilde{\omega}_2 + \tilde{\omega}_3}, \quad \text{for} \quad \tilde{\omega}_j = \frac{\gamma_j}{\left(\beta_j + \varepsilon\right)^2}.$$

The remaining parameters are set as [65]: $\gamma_1 = 1/10$, $\gamma_2 = 3/5$, $\gamma_3 = 3/10$, and $\varepsilon = 10^{-6}$. The calculation in the y direction proceeds in a similar way. The corresponding update of ϕ in 3D space is given in App. A.2 for completeness.

2.3. Lattice Boltzmann method for hydrodynamics

While the phase-field equation is solved using a finite-volume discretization as described above, the fluid equations are solved instead through a lattice Boltzmann solver based on a *velocity-based model* [67], which we further improve with a central-moment formulation to offer higher accuracy and stability in our two-phase flow simulation context. The fluid is thus represented through a

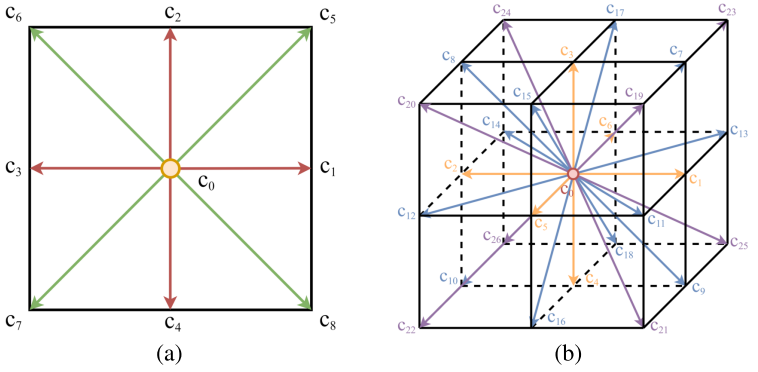

Fig. 2. The lattice structure D2Q9 (a) used in 2D, along with the lattice structure D3Q27 (b) used in 3D, where the vectors $\mathbf{c}_i$ are lattice velocities.

set of discrete probability distribution functions $\mathbf{g} = \{g_i\}$ of fluid particles on a regular grid, with a D2Q9 lattice structure in 2D and a D3Q27 structure in 3D (see Fig. 2). The discretization of the continuous Boltzmann transport equation reads as follows, at each node $\mathbf{x}_k$ of the regular grid:

$$g_i(\mathbf{x}_k + \mathbf{c}_i\delta t, t + \delta t) - g_i(\mathbf{x}_k, t) = \Omega_i^g(\rho, \mathbf{u}) + G_i(\rho, \mathbf{u}, \phi), \tag{22}$$

where the index i corresponds to the lattice velocity $\mathbf{c}_i$ (see App. A.1 for details); δt is the time step which is usually normalized to 1 in LBM; and G_i is the i-th component of the projection of the total force $\mathbf{F}$ composed of:

$$\mathbf{F} = \mathbf{F}_b + \mathbf{F}_s + \mathbf{F}_p + \mathbf{F}_\mu, \tag{23}$$

where $\mathbf{F}_p$ and $\mathbf{F}_\mu$ correspond respectively to the pressure gradient and the viscous force, evaluated using the method proposed in [67]; $\mathbf{F}_s$ and $\mathbf{F}_b$ are the surface tension and body forces appearing in Eq. (9). Aside from the last term, these forces depend on the phase-field gradient $\nabla\phi$ to properly couple the two fluids through interface dynamics.

While the collision $\mathbf{\Omega}^g = \{\Omega_i^g\}_i$ in Fakhari's work [67] uses a Weighted Multiple-Relaxation-Time (WMRT) collision model to improve over the original BGK model [9] for numerical stability and accuracy for flows at a higher Reynolds number, we instead rely on a high-order Central-Moment Multiple-Relaxation-Time (CM-MRT) collision model [15,68]: this numerical collision treatment better respects Galilean invariance and has been shown to be more accurate in single-phase fluid simulations [69] while generating promising results on two-phase flow simulations [70,71]. The collision components are expressed as (see App. A.3 for a thorough description):

$$\mathbf{\Omega}^g_{\text{CM-MRT}} = -\mathbf{M}^{-1}\mathbf{S}\mathbf{M}(\mathbf{g} - \mathbf{g}^{eq}), \tag{24}$$

where $\mathbf{M}$ is the central-moment projection matrix [15], and $\mathbf{M}^{-1}$ is its inverse which is analytically computed; $\mathbf{S}$ is the diagonal relaxation matrix [71], and $\mathbf{g}^{eq}$ is the Maxwell-Boltzmann equilibrium distribution expressed as:

$$g_i^{eq} = \Gamma_i + (p^* - 1)w_i - \frac{1}{2}G_i, \tag{25}$$

where p^* is the *normalized pressure* (related to the dimensionless pressure p through $p = \rho c_s^2 p^*$ with $c_s = 1/\sqrt{3}$ being the speed of sound); w_i refers to the i-th lattice weight (see App. A.1 for details), and Γ_i is expressed as:

$$\Gamma_i = w_i\left[1 + \frac{\mathbf{c}_i \cdot \mathbf{u}}{c_s^2} + \frac{1}{2}\left(\frac{\mathbf{c}_i \otimes \mathbf{c}_i}{c_s^2} - \mathbf{I}\right) : \frac{\mathbf{u}\mathbf{u}}{c_s^2}\right]. \tag{26}$$

Note that the variables p^* and $\mathbf{u}$ are computed through the moments of $\mathbf{g}$ via:

$$p^* = \sum_i g_i, \tag{27}$$

$$\mathbf{u} = \sum_i \mathbf{c}_i g_i + \frac{\mathbf{F}}{2\rho}. \tag{28}$$

Finally, the lattice Boltzmann equations in Eq. (22) are integrated via operator splitting, involving a collision step followed by a streaming step:

$$g_i^*(\mathbf{x}, t) = g_i(\mathbf{x}, t) + \Omega_i^g + G_i, \qquad \textit{(collision)} \tag{29}$$

$$g_i(\mathbf{x} + \mathbf{c}_i, t + 1) = g_i^*(\mathbf{x}, t), \qquad \textit{(streaming)} \tag{30}$$

where the asterisk denotes the (temporary) post-collision distribution functions.

Algorithm 1: Update of phase-field function and velocity field.

Initialize the values of density ρ, body force $\mathbf{F}_b$, surface tension force $\mathbf{F}_s$ and distribution distributions $\mathbf{g}$ based on the initial phase-field function ϕ and velocity field $\mathbf{u}$.
$t \leftarrow 0$.
repeat
  Update $\nabla\phi$ through Eq. (17).
  Update $\mathbf{n}$ through Eq. (7) to help with the wetting condition.
  Update $\mathbf{J}_2$ through Eq. (14).
  Update $\mathbf{J}_1$ through Eq. (19) and Eq. (21).
  Update the phase-field function value of each grid node (Eq. (13)).
  Compute the wetting boundary condition through Eq. (31).
  Update ρ through Eq. (10).
  Update $\mathbf{g}$ through Eq. (30).
  Update p^* through Eq. (27).
  Update $\mathbf{F}_b$, $\mathbf{F}_s$, $\mathbf{F}_p$ and $\mathbf{F}_\mu$ as described in Sec. 2.1 and Sec. 2.3.
  Update $\mathbf{u}$ as Eq. (28).
  Update Γ through Eq. (26).
  Update $\mathbf{g}^{eq}$ through Eq. (25).
  Update $\mathbf{\Omega}^g_{\text{CM-MRT}}$ through Eq. (24) with $\mathbf{M}$ as in Eq. (58).
  Set $\mathbf{S}$ as described in Sec. 2.3.
  Update $\mathbf{g}$ through Eqs. (29)-(30).
  $t \leftarrow t + 1$
until $t \geq T$;

The projection of the distribution functions into central-moment space enhances numerical stability and accuracy of the simulation, but other nonlinear spaces such as cumulants [17,19] can also be used, which are expected to have even higher accuracy and stability when carefully implemented for high Reynolds number flows. Since the study of collision modeling is not the focus of this paper, we leave it as future work.

2.4. Wetting boundary condition for phase-field equation

For the enforcement of boundary conditions near solid boundaries, various models to simulate wetting phenomena have been proposed to fix the phase-field function value ϕ_w at a solid boundary in order to control the gradient of the phase-field function along the boundary normal. In this work, we follow Jacqmin's contact model [72], which uses a boundary condition expressed as:

$$\mathbf{n}_w \cdot \nabla\phi\big|_{\mathbf{x}_w} = -\sqrt{\frac{2\beta}{\kappa}}\cos(\theta)\,\phi_w\left(1-\phi_w\right), \tag{31}$$

where ϕ_w is the phase-field function value at position $\mathbf{x}_w$ of the boundary wall interpolated from the ϕ values of the surrounding grid nodes, $\mathbf{n}_w$ is the normal of the solid boundary, and θ is the equilibrium contact angle. This condition offers a fine control over the hydrophobic ($\theta > \pi/2$) or hydrophilic ($\theta < \pi/2$) nature of the contact. The concrete discretization details of the wetting boundary condition are spelled out in [73], and we strictly follow them in our implementation.

2.5. Implementation

We implemented our hybrid LBM-FVM solver on GPU where a Structure-of-Array data layout is used for distribution functions to improve efficiency [74]. To reduce memory usage, we eliminate the need for intermediate temporary variables in the LBM updates (Eqs. (29)-(30)) by using the "in-place streaming" [48]. Our implementation thus requires a total of 15 floats per node in 2D space and 34 floats per node in 3D space. (Note that the density field ρ and velocity field $\mathbf{u}$ could be computed on the fly to further reduce memory usage, but we found convenient to store them as often done in other LBM implementations.) Whether in-place streaming is used or not, our approach saves memory through its use of an FVM-based treatment of the phase-field evolution compared to the existing two-phase fluid flow solvers based on DDF-LBM — especially for those employing a D3Q27 lattice structure for better rotational symmetry.

3. Numerical tests and validations

In this section, we present a number of numerical tests that we ran to evaluate our new hybrid LBM-FVM solver. We include tests with prescribed, spatially-varying vector fields to evaluate our FVM-based solution of the phase-field equation with a computation of the ℓ_2-norm of the relative error with respect to previous works [75]. We also compare our results on a number of common examples such as Rayleigh-Taylor instability and bubble rising with experimental measurements from previous works to assess quantitatively the accuracy of our method. Finally, we evaluate our simulations of 3D droplet coalescence when merged to a flat interface and of a 3D dam break example compared to a photography of an experiment to qualitatively measure the accuracy of our simulation.

In the following, unless stated, the dimensionless parameters of each example are defined as follows: the Reynolds number is $Re = U_0 L_0/\nu$ where U_0 is the reference flow speed and L_0 the characteristic dimension, while ν is the kinematic viscosity; the Péclet number is $Pe = U_0 L_0/M$ where M is the mobility; the Cahn number is $Ch = \xi/L_0$ where ξ is the interface width in the phase-field

(a) Initial circular interface profile (b) Circular interface profile after 10 cycles

Fig. 3. Diagonal translation of a circular interface at $Pe = 60$. Phase-field contours ($\phi = 0.5$) at $t = 0$ (a) and $t = 10T$ (b) are shown.

Table 1
Relative errors for the diagonal translation of a circular interface after a period of 10T using the setup in [44].

Approach	ϵ
Ours	0.0057
Ref. [44] (Zu and He)	0.1176
Ref. [44] (Geier's FD)	0.0074
Ref. [44] (Geier's Moments)	0.0874
Ref. [76] (DUGKS-I (WENO-Z5))	0.0064
Ref. [76] (DUGKS-II (WENO-Z5))	0.0064

Table 2
Relative errors for the Zalesak disk after a period of $2T$ at different Pe using the setup in [75].

Approach	Pe			
	80	400	800	4000
Ours	0.0566	0.0510	0.0517	0.0557
FD [75]	0.0593	0.0590	0.0558	0.0505
Moments [75]	0.0567	0.0482	0.0483	0.0501
Ref. [77] (Zu et al.)	0.1226	0.1186	0.1170	0.1194
Ref. [77] (Geier et al.)	0.1307	0.1224	0.1209	0.1472
Ref. [77] (Wang et al.)	0.1307	0.1224	0.1209	0.1471

model. By default, we set $M = 0.001$, $\xi = 3$ and $U_0 = 0.02$: these parameters correspond to a Mach number $Ma \approx 0.035$ — a value to avoid deleterious compressibility effects [75]. The time step of the FVM solver is given by $\Delta t = \chi \Delta x$ where χ controls the temporal step size with respect to the grid size. By default, we set $\chi = 1$, but it can be reduced for higher accuracy.

3.1. Diagonal translation of a circular interface

We consider the motion of a circular interface in a constant velocity field $\mathbf{u}_0 = (U_0, U_0)$, and adopt the setup found in [44]. Initially, a circular interface with radius $R = L_0/4$ is placed at the center of a square domain with a size $L_0 \times L_0$ where $L_0 = 100$, with $Pe = U_0 \xi / M = 60$. Periodic boundary conditions are used, and we set $\chi = 0.5$. The simulation is carried out until $t = 10T$ where $T = L_0/U_0$ is the full motion cycle after which the interface is expected to move back to its initial position. The accuracy of the method is evaluated by comparing the ℓ_2-norm of the relative phase-field error (denoted as ϵ) between the initial state and the state at the end of the simulation, i.e.,

$$\epsilon = \sqrt{\frac{\sum_{\mathbf{x}} (\phi_{10T} - \phi_0)^2}{\sum_{\mathbf{x}} \phi_0^2}}. \tag{32}$$

A visual representation of the initial interface (encoded by ϕ_0) and the one after a period of $10T$ (encoded via ϕ_{10T}) is shown in Fig. 3, while the errors ϵ for our method and five other existing methods are listed in Table 1. With the same setup and resolution, our method has the smallest error compared to other state-of-the-art methods, indicating higher accuracy of our FVM-based phase-field solver in this case.

3.2. Zalesak disk

The Zalesak disk test consists in a phase-field function in the shape of a slotted circular disk located at the center of a fluid field domain which is advected in a rotating fluid velocity prescribed as:

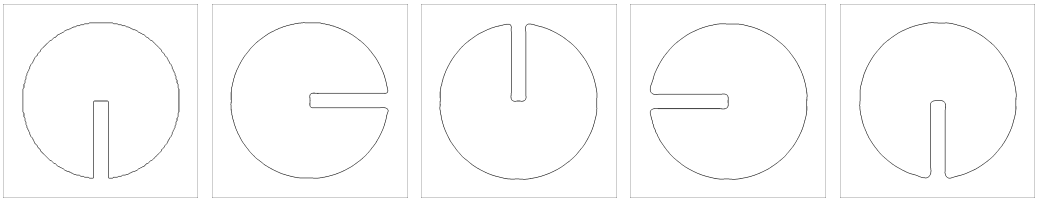

Fig. 4. Zalesak disk at $Pe = 800$: interface at (a) $t = 0$, (b) $t = 0.5T$, (c) $t = T$, (d) $t = 1.5T$, (e) $t = 2T$.

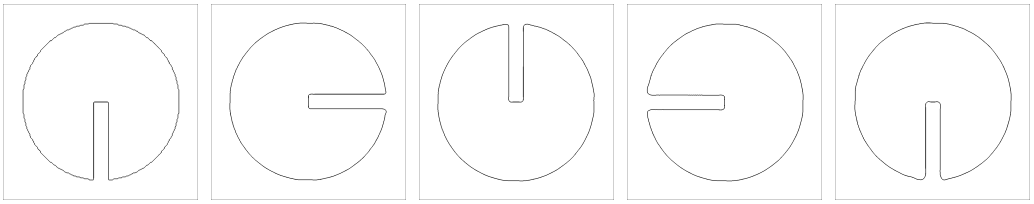

Fig. 5. Zalesak disk at $Pe = 4000$: interface at (a) $t = 0$, (b) $t = 0.5T$, (c) $t = T$, (d) $t = 1.5T$, (e) $t = 2T$.

Table 3
Relative errors of a deforming circular interface in a smooth shear flow after a period of $2T$ using the setup in [75].

Model	ε
Ours	0.0138
FD [75]	0.0199
Mom [75]	0.0204
Ref. [77] (Zu et al.)	0.0125
Ref. [77] (Geier et al.)	0.0136
Ref. [77] (Wang et al.)	0.0139

$$u_x = -U_0 2\pi \left(\frac{y}{L_0} - 0.5 \right),$$
$$u_y = U_0 2\pi \left(\frac{x}{L_0} - 0.5 \right). \tag{33}$$

After a period of time $T = L_0/U_0$, the disk should return to its initial position with its original shape if the numerical advection is error-free. In our experiment, the radius of the disk is set to $R = 80$, and the fluid domain size is of $L_0 \times L_0$ with $L_0 = 200$. The width of the slot is set to 15 grid cells, and the Cahn number Ch here is set to 0.01 (corresponding to an interface width $\xi = 2$). The ℓ_2 error between the initial disk and the isovalue $1/2$ of the phase-field function after a full revolution is measured for our FVM-based phase-field solver and reported in Table 2, along with other existing methods. Our results are on par with the latest work of De Rosis and Enan [75], despite our reduced memory footprint. We visualize our results for $Pe = 800$ and $Pe = 4000$ in Fig. 4 and Fig. 5, respectively. We note that the errors are smaller for $Pe = 400$ and $Pe = 800$, showing that the mobility parameter M affects the accuracy of this experiment — which is consistent with the results previously reported in [75,77].

3.3. Deformation of a circular interface in a smoothed shear flow

To further test the capacity of our solver in capturing interface deformation, we consider a common benchmark test where the interface undergoes a large deformation in a smooth shear flow. For a square domain of size $L_0 \times L_0$ with $L_0 = 512$, and an interface width $\xi = 2$, a circularly shaped interface having a radius of $R = L_0/5$ is placed at the center of the domain and driven by a smooth, time-dependent and non-linear flow field defined as:

$$u_x = -U_0 \sin\left(4\pi \frac{x}{L_0}\right) \sin\left(4\pi \frac{y}{L_0}\right) \cos\left(4\pi \frac{t}{T}\right),$$
$$u_y = -U_0 \cos\left(4\pi \frac{x}{L_0}\right) \cos\left(4\pi \frac{y}{L_0}\right) \cos\left(4\pi \frac{t}{T}\right). \tag{34}$$

The period for this case is set to $T = L_0/U_0$, corresponding to the time that the interface should recover its original shape, and we use $\chi = 0.5$. As shown in Table 3, the error achieved by our method is on par to that of the other methods. The interface evolution

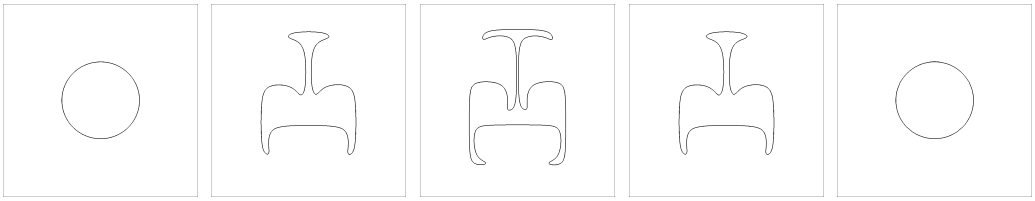

Fig. 6. Deformation of a circular interface in a smooth shear flow: interface at (a) $t = 0$, (b) $t = 0.5T$, (c) $t = T$, (d) $t = 1.5T$, (e) $t = 2T$.

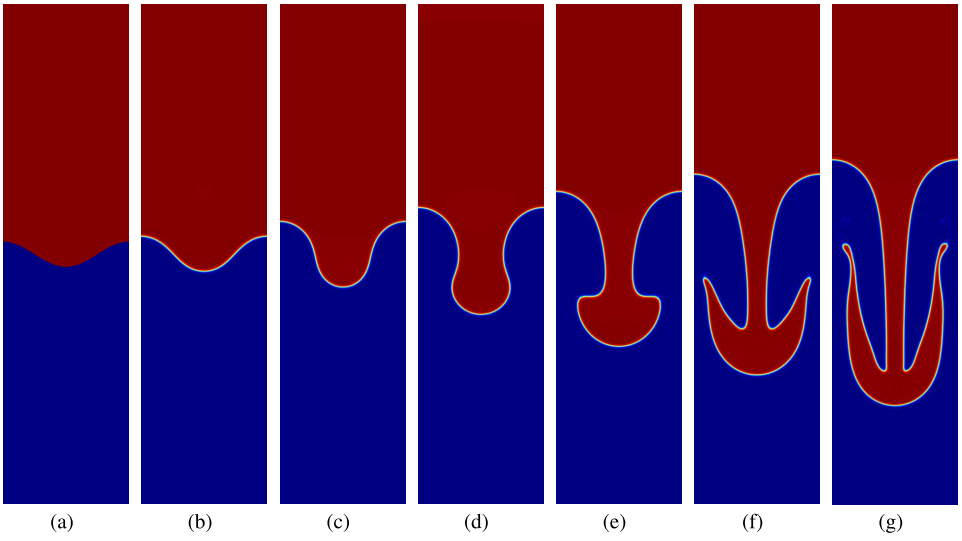

Fig. 7. 2D Rayleigh Taylor instability at $Re = 256$.

for our approach over a period is shown in Fig. 6. At time $t = T/2$, the largest shape change of the interface takes place (exhibiting a thin filament structure in the middle of the domain), consistent with reported results in other works [75,59,44,78,79,77].

3.4. 2D Rayleigh-Taylor instability

Another popular benchmark test case is the Rayleigh–Taylor instability, which tests the ability of a numerical scheme to tackle a system composed of two immiscible fluids for more complex interactions. Here, the heavier fluid is initially placed on the top. A rectangular domain of size $L_0 \times 4L_0$ where $L_0 = 256$ is used, with the boundary of the two fluids initialized as:

$$\phi(\mathbf{x}, t = 0) = \phi_H, \quad \text{if } y > 2L_0 + 0.1L_0 \cos\left(2\pi \frac{x}{L_0}\right),$$
$$\phi(\mathbf{x}, t = 0) = \phi_L, \quad \text{otherwise.} \tag{35}$$

Boundary conditions for the vertical walls are set as periodic, while the top and bottom boundaries enforce no-slip boundary conditions. Gravity is set to $\mathbf{g} = (0, -g, 0)$, where $g = U_0^2/L_0$ and $U_0 = 0.04$. The interface width is set to $\xi = 5$. The viscosity is set from the Reynolds number, i.e., it is defined as $\nu = L_0\sqrt{gL_0}/Re$. The Atwood number, defined as $A_t = (\rho_H - \rho_L)/(\rho_H + \rho_L)$, is set to 0.5, with $\rho_L = 1$. The capillarity number, defined as $Ca = \mu_H U_0/\sigma$, is set to 0.26. The Péclet number is set to 500. Visualization of our results for $Re = 256$, 3000, and 30000 are shown in Figs. 7, 8 and 9, respectively. To assess the accuracy of our solver, the time evolution of both the bubble front and its spike tip (see Figs. 10) are tracked, and compared to previous experimental results [42,80,76,81] as listed in [67,53]. The evolution of the spike position $y^\dagger$ of the interface normalized by the width of the domain L_0 for the three different Reynolds numbers are given in Table 4. They agree with the results reported in previous works, see, for instance, [42,82–84]. As the Reynolds number grows, the breakup of the phase tail into multiple droplets becomes more prominent in the tail. These droplets are generated from the rolling-up tail of the interface around $t = 2.5T$, where T is defined as $T = \sqrt{L_0/(g \cdot A_t)}$. These features are also on par with previous findings [42,83,85].

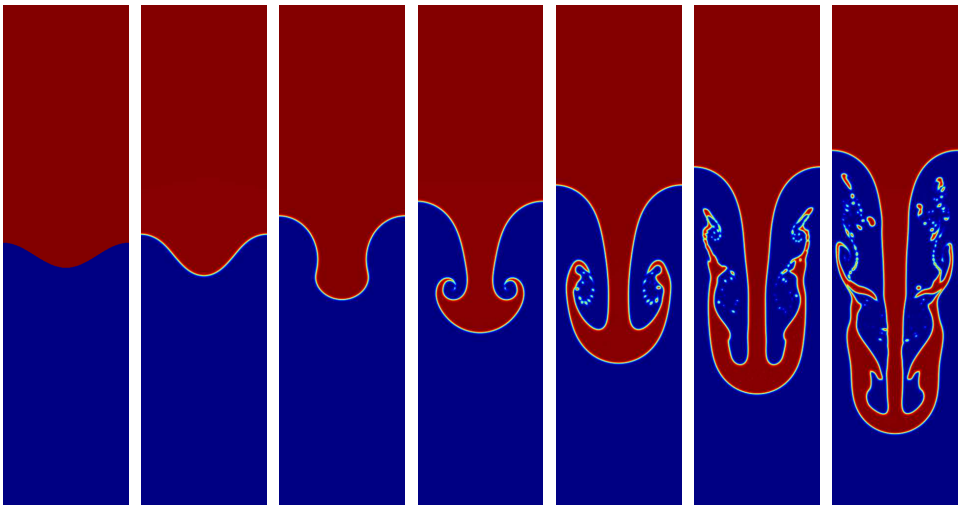

Fig. 8. 2D Rayleigh Taylor instability at $Re = 3000$.

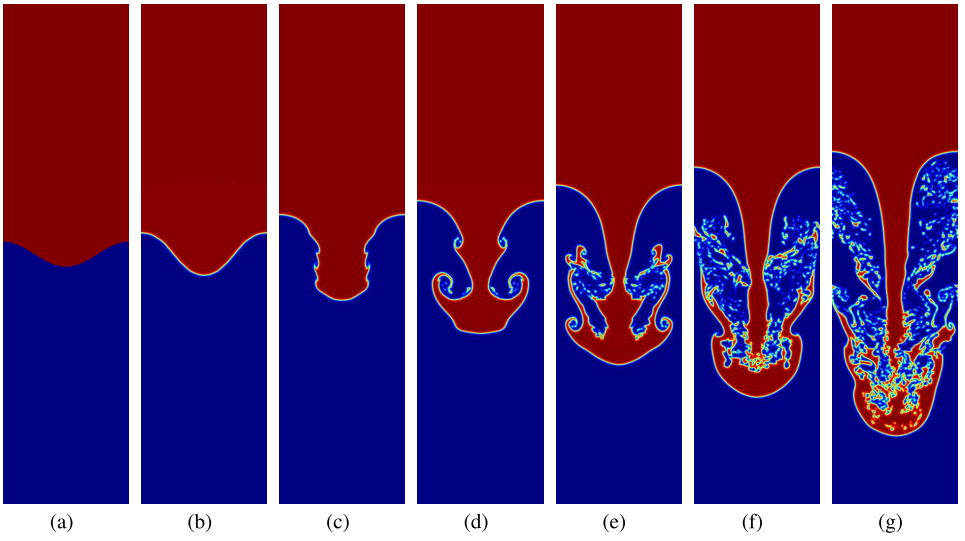

Fig. 9. 2D Rayleigh Taylor instability at $Re = 30000$.

Table 4
2D Rayleigh–Taylor instability at $Re = 256$, $Re = 3000$ and $Re = 30000$: vertical position of the spike of the interface normalized by the width of the domain at representative times.

t/T	0	0.5	1.0	1.5	2	2.5	3.0
$y^{\dagger}$ at $Re = 256$:	1.900	1.859	1.734	1.516	1.258	1.031	0.781
$y^{\dagger}$ at $Re = 3000$:	1.900	1.832	1.645	1.383	1.137	0.887	0.574
$y^{\dagger}$ at $Re = 30000$:	1.900	1.828	1.629	1.367	1.117	0.852	0.559

Table 5
3D Rayleigh–Taylor instability at $Re = 256$, $Re = 3000$ and $Re = 30000$: vertical position of the spike of the interface normalized by the width of the domain at representative times.

t/T	0	0.5	1.0	1.5	2	2.5	3.0
$y^{\dagger}$ at $Re = 256$:	1.904	1.844	1.766	1.609	1.406	1.141	0.859
$y^{\dagger}$ at $Re = 3000$:	1.904	1.844	1.75	1.547	1.297	0.984	0.641
$y^{\dagger}$ at $Re = 30000$:	1.904	1.844	1.734	1.547	1.281	0.938	0.531

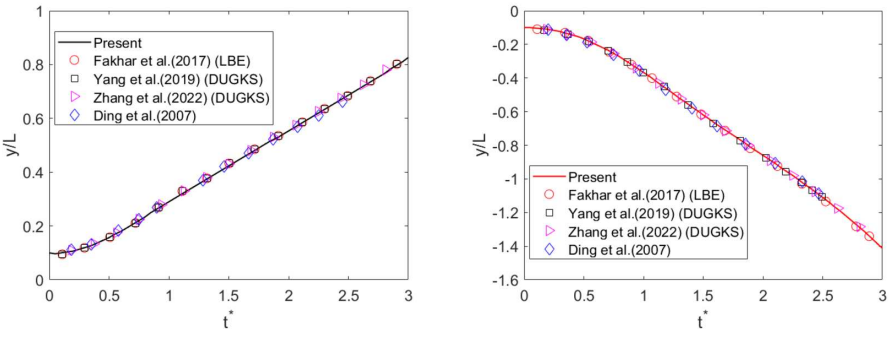

Fig. 10. Comparisons of the (a) bubble front and (b) spike tip positions at $Re = 3000$, $At = 0.5$, $Pe = 1000$ and $\mu_h/\mu_l = 1$ for various numerical techniques.

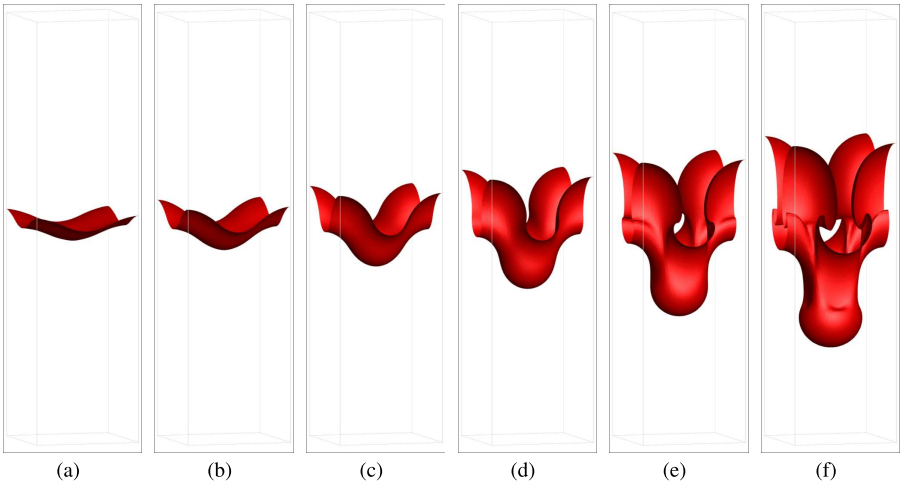

Fig. 11. 3D Rayleigh Taylor Instability at $Re = 256$.

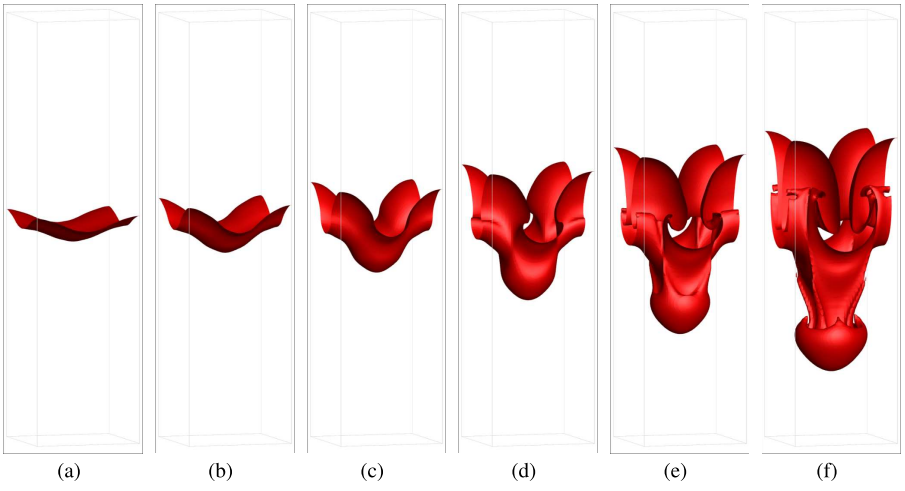

Fig. 12. 3D Rayleigh Taylor Instability at $Re = 3000$.

3.5. 3D Rayleigh-Taylor instability

We also tested the Rayleigh-Taylor instability in a 3D domain, for a size $L_0 \times 4L_0 \times L_0$ with $L_0 = 64$, and with the boundary of the two immiscible fluids initialized as

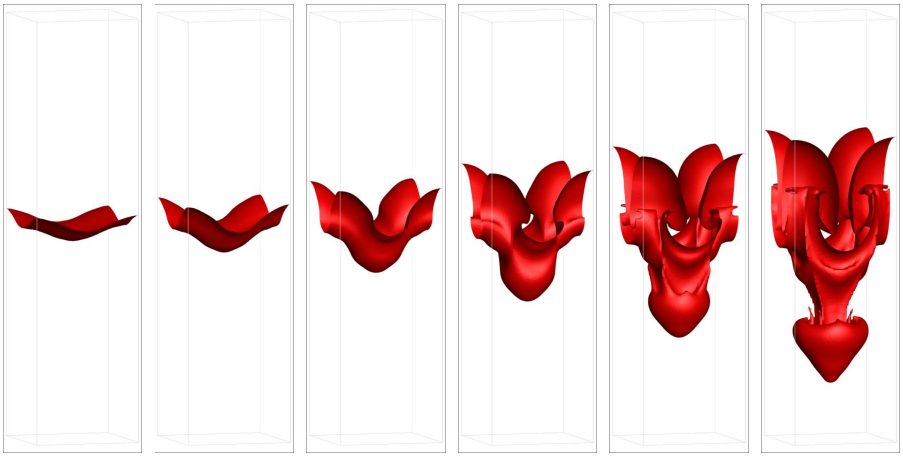

Fig. 13. 3D Rayleigh Taylor instability at $Re = 30000$.

Table 6
3D Rayleigh–Taylor instability at $Re = 256$: vertical position of the interface spike normalized by the domain width at representative times (values taken from [75]).

t/T	[70]	[71]	[87]	[88]	Ours
0.0	1.897	1.897	1.895	1.904	1.904
0.5	1.897	1.897	1.864	1.869	1.844
1.0	1.753	1.753	1.763	1.776	1.766
1.5	1.592	1.591	1.587	1.618	1.609
2.0	1.381	1.378	1.357	1.396	1.406
2.5	1.126	1.121	1.085	1.149	1.141
3.0	0.844	0.791	0.788	0.863	0.859

$$\phi(\mathbf{x}, t=0) = \phi_H, \quad \text{if } y > 2L_0 + 0.05L_0\left[\cos\left(2\pi\frac{x}{L_0}\right) + \cos\left(2\pi\frac{z}{L_0}\right)\right],$$
$$\phi(\mathbf{x}, t=0) = \phi_L, \quad \text{otherwise.} \tag{36}$$

The governing dimensionless parameters are set to: $At = 0.5$, $Ca = 960$ and $Pe = 256$. Gravity is set to $\mathbf{g} = (0, -g, 0)$, where $g = U_0^2/L_0$ and $U_0 = 0.04$. Interface width is set to $\xi = 5$, and viscosity is set to $\nu = L_0\sqrt{gL_0}/Re$. The reference time scale T is defined as $T = \sqrt{L_0/g}$. Visualization of the results for $Re = 256$ is shown in Fig. 11. The light fluid rises up to form a bubble and the heavy fluid drops to generate a mushroom-shaped spike. At time $t = 2T$, we observe that the first roll-up of the heavy fluid appears close to the saddle points, which comes from the presence of a Kelvin-Helmholtz instability. These observations are consistent with the tests described in [86]. The vertical positions of the spike at different times for $Re = 256$, $Re = 3000$ and $Re = 30000$ are shown in Table 5; once again, they are in agreement with previous works [70,71,87,88], for which the quantitative results are reported in Table 6 for comparison purposes. Visualizations of the interface at different times for $Re = 3000$ and $Re = 30000$ are shown in Figs. 12 and 13, respectively.

3.6. 2D bubble rising

We now consider the simulation of a rising bubble in 2D. This buoyancy-driven benchmark test used in many scientific and engineering applications [89,90] involves a two-phase flow problem where a bubble is made of a light fluid which is surrounded by a denser fluid. The bubble thus naturally rises in the dense fluid. We tested two different cases, characterized by two dimensionless numbers which are the Reynolds number (Re) and Eötvos number (Eo), defined as:

$$Re = \frac{\rho_H D\sqrt{gD}}{\nu_H}, \qquad Eo = \frac{\rho_H g D^2}{\sigma}, \tag{37}$$

where D is the initial diameter of the bubble and σ is the surface tension [91]. In order to quantify the dynamics of the bubble during rising, the rising velocity and center of mass of the bubble are measured respectively by

$$y_c = \frac{\int_{\phi<0.5(\phi_H+\phi_L)} \phi d\mathbf{x}}{\int_{\phi<0.5(\phi_H+\phi_L)} 1 d\mathbf{x}}, \tag{38}$$

Table 7
Physical parameters and dimensionless numbers for two test cases of bubble rising.

Test Case	ρ_H	ρ_L	ν_H	ν_L	Re	Eo	ρ_H/ρ_L
1	1	0.1	0.01	0.01	35	10	10
2	1	0.001	0.01	0.1	35	125	1000

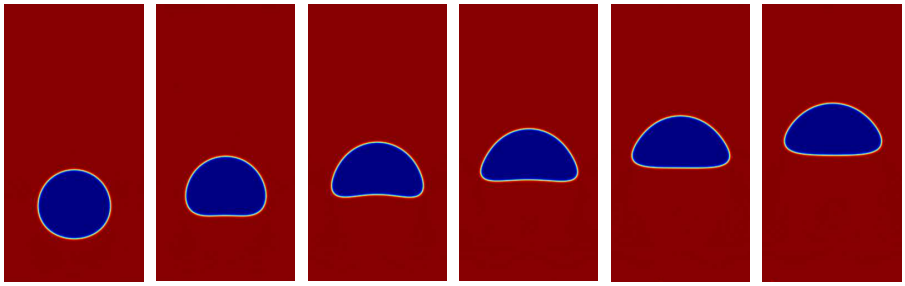

Fig. 14. 2D bubble rising for case 1.

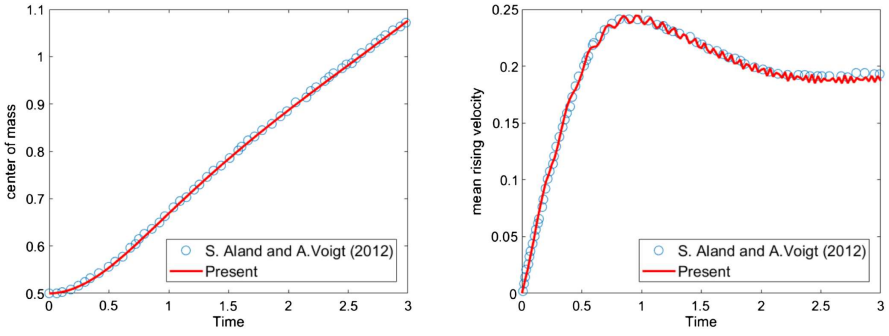

(a) Center of mass (b) Rising Velocity

Fig. 15. Comparison to the numerical results from [92] for the case 1 of bubble rising, with a density ratio of 10. (a) Time evolution of the bubble's center of mass, and (b) of its mean rising velocity.

$$u_c = \frac{\int_{\phi<0.5(\phi_H+\phi_L)} u_y(\mathbf{x})d\mathbf{x}}{\int_{\phi<0.5(\phi_H+\phi_L)} 1d\mathbf{x}}. \tag{39}$$

The first test (case 1) sets $Re = 35$ and $Eo = 10$, which should produce an ellipsoidal bubble; the second test (case 2) sets $Re = 35$ and $Eo = 125$, which should produce a bubble in the ellipsoidal-cap regime. In both cases, the domain has a size of $L \times 2L$, and the simulation parameters are set to $L = 240$, $U_0 = 0.001944$, $M = 0.005$, $\chi = 0.125$ and $\xi = 4$. Surface tension and viscosity are determined by Eo and Re. The complete list of physical parameters for the two cases are given in Table 7, and their results are shown in Figs. 14, 15, 16 and 17. In Figs. 14 and 16, we show the bubble evolution at every $T/2$ time interval (where $T = \sqrt{2L_0/g}$) for two different Eo numbers. To further verify the accuracy of our solver, we measure the center of mass y_c by Eq. (38) and the rising velocity by Eq. (39) for case 1 and case 2, respectively: Figs. 15 and 17 plot these measurements, proving good agreement with existing solvers [92,93].

3.7. 3D droplet coalescence with a flat interface

We also simulate a droplet coalescence with an initially flat interface [52,94], a well-studied phenomenon governed by interface tension, gravity, and viscous forces. The computational domain is set to $2L_0 \times 2L_0 \times 2L_0$ with $L_0 = 100$, and the flat liquid interface is set to L_0 in the y direction. A spherical droplet of diameter $D = L_0/3$ is positioned at $(L_0, \frac{7}{6}L_0 + \delta, L_0)$, where δ is the gap distance between the droplet and the flat interface. The density ratio is set to $\rho^* = \rho_H/\rho_L = 1.316$, and the dimensionless parameters (which mostly influence the coalescence phenomenon [52,94]) are set to $\mu^* = 0.5$, $\mathrm{Bo} = 9.59 \times 10^{-2}$ and $\mathrm{Oh} = 5.53 \times 10^{-3}$, where the Bond number Bo is defined as

$$\mathrm{Bo} = \frac{g_y\left(\rho_H - \rho_L\right) D^2}{\sigma}, \tag{40}$$

with $\sigma = 1.8 \times 10^{-4}$, while the Ohnesorge number Oh is

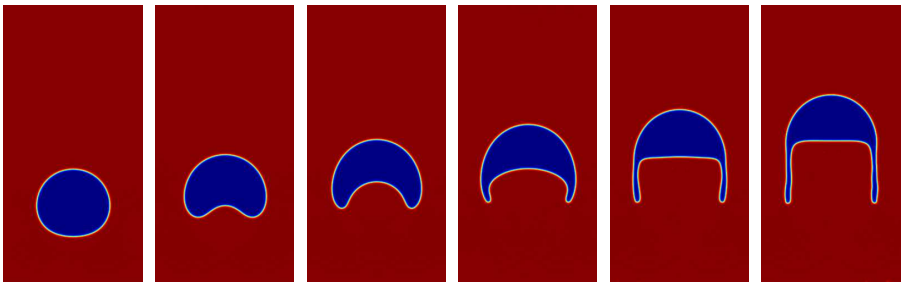

Fig. 16. 2D bubble rising for case 2.

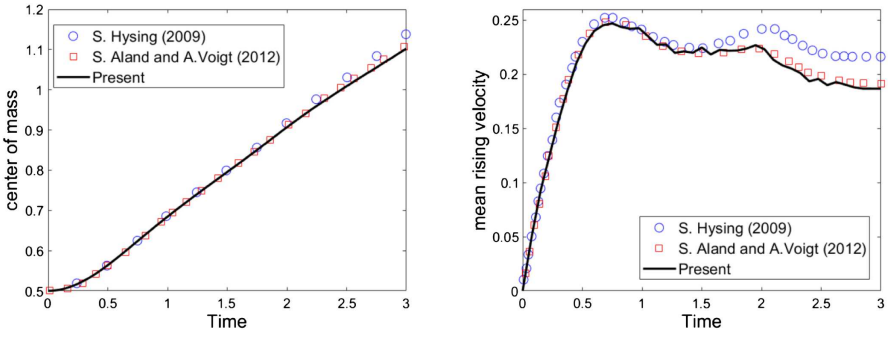

(a) Center of mass (b) Rising Velocity

Fig. 17. Comparison to the numerical results from [92,93] for the case 2 of bubble rising, with a density ratio of 1000. (a) Time evolution of the bubble's center of mass, and (b) of its mean rising velocity.

Table 8
Comparison of computing time across different grid resolutions between the DDF-LBM approach and our hybrid method for a simulation time up to $3T$, where T is the reference time defined in Section 3.5.

Grid Resolution	$64 \times 256 \times 64$	$128 \times 512 \times 128$	$256 \times 1024 \times 256$
DDF-LBM (D3Q27)	19 s	284 s	4590 s
Our LBM-FVM solver	13 s	185 s	3033 s

$$\mathrm{Oh} = \frac{\mu_H}{\sqrt{\rho_H \sigma D}}. \tag{41}$$

Gravity is set to $g_y = 5 \times 10^{-7}$ in the vertical direction; interface width is set to $\xi = 3$, and mobility is set to 0.1. A visualization of our result is provided in Fig. 18, showing good agreement with the snapshots of an experiment performed in [94] taken at various dimensionless times $t^* = t/t_c$ where $t_c = \sqrt{\rho_H D^3/\sigma}$ is the capillary time. Our results are thus consistent with previous numerical and experiment observations [52,94].

3.8. 3D dam break against rectangular pillar

Finally, we compare a simulation of a dam break in 3D using our solver to a corresponding experiment [95], for the setup shown in Fig. 19. We use a fluid domain of size $4L \times 3L \times L$ for $L = 180$. The physical parameters are set to $g = 5 \times 10^{-6}$, $\sigma = 5 \times 10^{-7}$, $\nu_L = 0.05$, $\nu_H = 27/Re$, $\xi = 5$ and $M = 0.1$. We use $T = \sqrt{4L/g}$ as a reference time scale. Density ratio is set to $\gamma = 800$, and the Reynolds number is set to $Re = 20000$. A visualization of our results is shown in Fig. 20, demonstrating reasonable visual agreement with snapshots taken from the photograph of the experiment.

3.9. Discussions

The numerical tests we presented above proved that our solver is often at the same level of accuracy, and sometimes even better, than the existing two-phase flow simulation methods using either DDF-LBM or DUGKS — even if our solver requires less memory compared to both types of methods. Moreover, our method can freely adapt the time step or the WENO order of our FVM-based phase-field solver to achieve higher accuracy for interface evolution. In addition, our approach runs with an efficiency at least

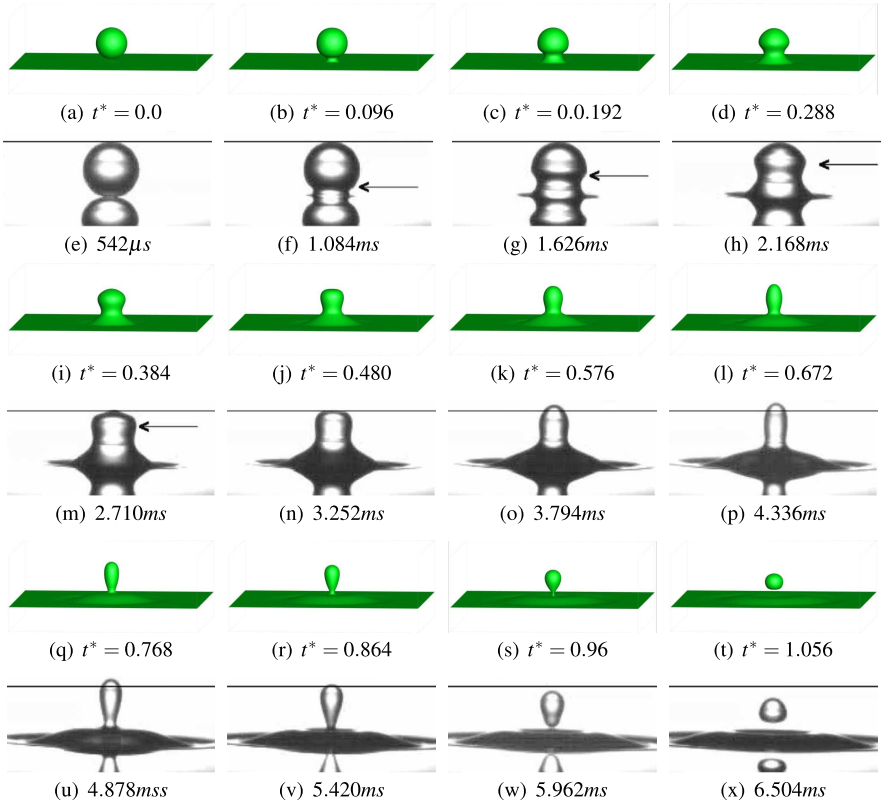

Fig. 18. 3D droplet coalescence with a flat interface where $\rho^* = 1.316$, $\mu^* = 0.5$, $\mathrm{Bo} = 9.59 \times 10^{-2}$ and $\mathrm{Oh} = 5.53 \times 10^{-3}$. The isosurface $\phi = 0.5$ is shown in green, and compared with the experiment from [94] at a time interval of 542 μs.

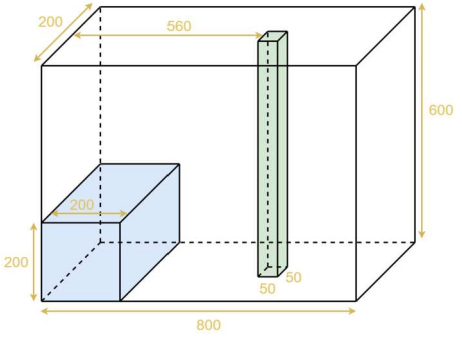

Fig. 19. The experimental setup of a 3D dam break against a rectangular pillar from [95].

equivalent, and sometimes higher than existing methods due to reduced memory access, especially when a GPU implementation is used. Table 8 shows a comparison of performance for the simulation of a 3D Rayleigh-Taylor instability using different grid resolutions between the DDF-LBM method (a 3D implementation of [67] where a raw-moment MRT collision model is employed and a rotationally symmetric D3Q27 lattice structure is used for both the fluid flow and phase-field equations) and our hybrid LBM-FVM solver. Our reduced use of memory leads to more than 30% improvement in computational efficiency. Note that the DDF-LBM we implemented does not match the accuracy of our method since a cheaper collision model is involved; it would become even slower if a similar accuracy is enforced through the use of a higher-order collision model. The DUGKS solver [53] is even slower, although its accuracy is higher than the DDF-LBM approach. This example highlights the fact that our new LBM-FVM solver is a viable alternative for high-performance, high-accuracy simulations of high-resolution two-phase flows, particularly when a restricted memory size is available. We acknowledge the drawback that the use of a high-order WENO scheme involves a larger stencil size, which could induce more discontinuous memory access, thus potentially slowing down computations; it would also require more careful handling of boundaries. However, the larger stencil issue could be potentially alleviated through adopting a compact high-order method such as [96]. In any case, our work provides a conservative and low-memory discretization of the phase-field equation with a higher order, which could be the only practical approach to accurate *multiphase fluid* simulations if limited memory is available.

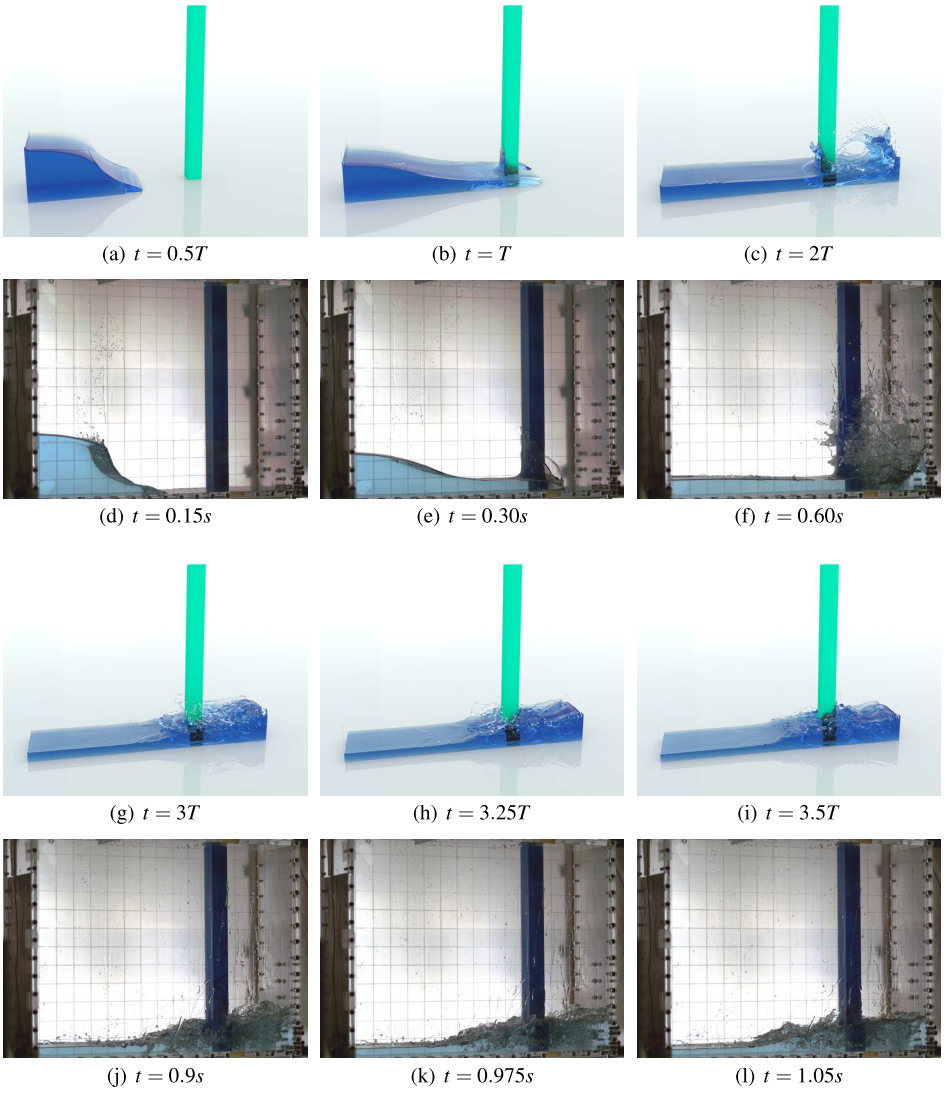

Fig. 20. Qualitative validation of 3D dam break against a rectangular pillar at $Re = 20000$ with $\gamma = 800$, compared to the photograph of an experiment from [95].

4. Conclusion

In this paper, we propose a hybrid method to solve the coupled phase-field and lattice Boltzmann equations for two-phase flow simulations. Unlike existing DDF-LBM solvers, we couple a conservative finite-volume solver for the phase-field equation with a high-order lattice Boltzmann solver for fluid equations. We showed that our numerical treatment to evolve the phase-field equation matches or exceeds previous works due to our selection of a WENO-5 advection to avoid spurious oscillations around the interface, and of an isotropic second-order scheme for the phase-field gradient needed in coupling terms. The use of velocity-based collision model for solving fluid equations is also very important to suppress pressure oscillations in order to achieve higher accuracy. Combined with our LBM integration based on a high-order central-moment multiple-relaxation-time collision model, the resulting hybrid solver was shown to simulate two-phase flows accurately for a series of benchmark test cases. More importantly, the memory requirement for our FVM-based phase-field evolution is reduced compared to the usual DDF-LBM or DUGKS solvers for the phase-field equation. As a consequence, our solver can easily handle larger-scale, high-resolution two-phase flow simulations with a restricted memory size, while retaining similar or even higher accuracy than LBM methods that are purely based on distribution functions.

CRediT authorship contribution statement

Yihui Ma: Methodology, Software, Validation. **Xiaoyu Xiao:** Software, Validation. **Wei Li:** Methodology, Supervision, Writing – original draft. **Mathieu Desbrun:** Methodology, Supervision, Writing – original draft, Writing – review & editing. **Xiaopei Liu:** Methodology, Supervision, Validation, Writing – original draft, Writing – review & editing.

Declaration of competing interest

The authors declare that they have no known competing financial interests or personal relationships that could have appeared to influence the work reported in this paper.

Data availability

The authors do not have permission to share data.

Acknowledgement

This work was supported by the National Natural Science Foundation of China (No. 62072310), the generous support from ShanghaiTech University and a Choose France Inria chair, as well as the partial funding from Ansys and Adobe Research.

Appendix A

A.1. Lattice velocity sets

The lattice velocity set of a D2Q9 lattice structure (Fig. 2, left) is:

$$\begin{aligned}\mathbf{c}_x &= [0,1,0,-1,0,1,-1,-1,1]^\top,\\ \mathbf{c}_y &= [0,0,1,0,-1,1,1,-1,-1]^\top,\end{aligned} \tag{42}$$

and the fixed lattice weights are

$$w = \left[\frac{4}{9},\frac{1}{9},\frac{1}{9},\frac{1}{9},\frac{1}{9},\frac{1}{36},\frac{1}{36},\frac{1}{36},\frac{1}{36}\right]^\top. \tag{43}$$

The lattice velocity set for a D3Q27 lattice structure (Fig. 2, right) is:

$$\begin{aligned}\mathbf{c}_x &= [0,1,-1,0,0,0,0,1,-1,1,-1,1,-1,1,\\ &\quad -1,0,0,0,0,1,-1,1,-1,1,-1,1,-1]^\top,\\ \mathbf{c}_y &= [0,0,0,1,-1,0,0,1,1,-1,-1,0,0,0,\\ &\quad 0,1,-1,1,-1,1,1,-1,-1,1,1,-1,-1]^\top,\\ \mathbf{c}_z &= [0,0,0,0,0,1,-1,0,0,0,0,1,1,1,\\ &\quad -1,1,1,-1,-1,1,1,1,1,-1,-1,-1,-1]^\top,\end{aligned} \tag{44}$$

and the fixed lattice weights are

$$\begin{aligned}w = \Big[&\frac{8}{27},\frac{2}{27},\frac{2}{27},\frac{2}{27},\frac{2}{27},\frac{2}{27},\frac{2}{27},\frac{1}{54},\frac{1}{54},\\ &\frac{1}{54},\frac{1}{54},\frac{1}{54},\frac{1}{54},\frac{1}{54},\frac{1}{54},\frac{1}{54},\frac{1}{54},\frac{1}{54},\frac{1}{54},\\ &\frac{1}{216},\frac{1}{216},\frac{1}{216},\frac{1}{216},\frac{1}{216},\frac{1}{216},\frac{1}{216},\frac{1}{216}\Big]^\top.\end{aligned} \tag{45}$$

A.2. Finite-volume solver for the phase-field equation in 3D

The update of a phase-field function value $\phi_{i,j,k}$ at a grid node (i,j,k) is:

$$\begin{aligned}&\frac{\phi_{(i,j,k),t+1}-\phi_{(i,j,k),t}}{\Delta t} =\\ &= M\cdot\Big(\nabla\phi_{i+\frac{1}{2},j,k}-\nabla\phi_{i-\frac{1}{2},j,k}+\nabla\phi_{i,j+\frac{1}{2},k}\\ &-\nabla\phi_{i,j-\frac{1}{2},k}+\nabla\phi_{i,j,k+\frac{1}{2}}-\nabla\phi_{i,j,k-\frac{1}{2}}\Big)\Delta x\\ &+[\,M\cdot\frac{4}{\xi}\left(\phi_{(i+\frac{1}{2},j,k),t}\left(1-\phi_{(i+\frac{1}{2},j,k),t}\right)\mathbf{n}_{(i+\frac{1}{2},j,k),t}\right)\\ &-M\cdot\frac{4}{\xi}\left(\phi_{(i-\frac{1}{2},j,k),t}\left(1-\phi_{(i-\frac{1}{2},j,k),t}\right)\mathbf{n}_{(i-\frac{1}{2},j,k),t}\right)\end{aligned} \tag{46}$$

$$
\begin{aligned}
&+ M \cdot \frac{4}{\xi}\left(\phi_{(i,j+\frac{1}{2},k),t}\left(1-\phi_{(i,j+\frac{1}{2},k),t}\right)\mathbf{n}_{(i,j+\frac{1}{2},k),t}\right)\\
&- M \cdot \frac{4}{\xi}\left(\phi_{(i,j-\frac{1}{2},k),t}\left(1-\phi_{(i,j-\frac{1}{2},k),t}\right)\mathbf{n}_{(i,j-\frac{1}{2},k),t}\right)\\
&+ M \cdot \frac{4}{\xi}\left(\phi_{(i,j,k+\frac{1}{2}),t}\left(1-\phi_{(i,j,k+\frac{1}{2}),t}\right)\mathbf{n}_{(i,j,k+\frac{1}{2}),t}\right)\\
&- M \cdot \frac{4}{\xi}\left(\phi_{(i,j,k-\frac{1}{2}),t}\left(1-\phi_{(i,j,k-\frac{1}{2}),t}\right)\mathbf{n}_{(i,j,k-\frac{1}{2}),t}\right)\Big]\Delta x\\
&-\Big(\mathbf{J}_{1,(i+\frac{1}{2},j,k),t}\cdot\begin{pmatrix}1\\0\\0\end{pmatrix}+\mathbf{J}_{1,(i-\frac{1}{2},j,k),t}\cdot\begin{pmatrix}-1\\0\\0\end{pmatrix}+\mathbf{J}_{1,(i,j+\frac{1}{2},k),t}\cdot\begin{pmatrix}0\\1\\0\end{pmatrix}\\
&+\mathbf{J}_{1,(i,j-\frac{1}{2},k),t}\cdot\begin{pmatrix}0\\-1\\0\end{pmatrix}+\mathbf{J}_{1,(i,j,k+\frac{1}{2}),t}\cdot\begin{pmatrix}0\\0\\1\end{pmatrix}+\mathbf{J}_{1,(i,j,k-\frac{1}{2}),t}\cdot\begin{pmatrix}0\\0\\-1\end{pmatrix}\Big)\Delta x,
\end{aligned}
$$

where the phase-field function value at point $(i+1/2,j,k)$ is interpolated from neighboring nodes through

$$\phi_{i+\frac{1}{2},j,k}=\left(\phi_{i+1,j,k}+\phi_{i,j,k}\right)/2, \tag{47}$$

and phase-gradient terms such as $\nabla\phi_{i+\frac{1}{2},j,k}$ are calculated through central differences. For phase interface normals $\mathbf{n}_{i+\frac{1}{2},j,k}$, we use a linear interpolation scheme: for instance,

$$
\begin{aligned}
\mathbf{n}_{i+\frac{1}{2},j,k}&=\left(\mathbf{n}_{i+1,j,k}+\mathbf{n}_{i,j,k}\right)/2\\
&=\left(\frac{\nabla\phi_{i+1,j,k}}{\|\nabla\phi_{i+1,j,k}\|}+\frac{\nabla\phi_{i,j,k}}{\|\nabla\phi_{i,j,k}\|}\right)/2,
\end{aligned}\tag{48}
$$

where the phase-field gradients are also computed using the second-order isotropic central scheme [52], that is,

$$\nabla\phi=3\sum_i w_i\mathbf{c}_i\frac{\phi(\mathbf{x}+\mathbf{c}_i\delta t)-\phi(\mathbf{x})}{\Delta x}. \tag{49}$$

For $\mathbf{J}_1$ in the 3D field, the discrete form of the surface integral around a grid node is:

$$
\begin{aligned}
&\mathbf{J}_{1,(i+\frac{1}{2},j,k),t}\cdot\begin{pmatrix}1\\0\\0\end{pmatrix}+\mathbf{J}_{1,(i-\frac{1}{2},j,k),t}\cdot\begin{pmatrix}-1\\0\\0\end{pmatrix}+\mathbf{J}_{1,(i,j+\frac{1}{2},k),t}\cdot\begin{pmatrix}0\\1\\0\end{pmatrix}\\
&+\mathbf{J}_{1,(i,j-\frac{1}{2},k),t}\cdot\begin{pmatrix}0\\-1\\0\end{pmatrix}+\mathbf{J}_{1,(i,j,k+\frac{1}{2}),t}\cdot\begin{pmatrix}0\\0\\1\end{pmatrix}+\mathbf{J}_{1,(i,j,k-\frac{1}{2}),t}\cdot\begin{pmatrix}0\\0\\-1\end{pmatrix}\\
&=\phi_{(i+\frac{1}{2},j,k),t}u_{x,(i+\frac{1}{2},j,k),t}-\phi_{(i-\frac{1}{2},j,k),t}u_{x,(i-\frac{1}{2},j,k),t}\\
&+\phi_{(i,j+\frac{1}{2},k),t}u_{y,(i,j+\frac{1}{2},k),t}-\phi_{(i,j-\frac{1}{2},k),t}u_{y,(i,j-\frac{1}{2},k),t}\\
&+\phi_{(i,j,k+\frac{1}{2}),t}u_{z,(i,j,k+\frac{1}{2}),t}-\phi_{(i,j,k-\frac{1}{2}),t}u_{z,(i,j,k-\frac{1}{2}),t},
\end{aligned}\tag{50}
$$

where the values of $\mathbf{u}$ at $(i+1/2,j,k)$ are evaluated as

$$\mathbf{u}_{i+\frac{1}{2},j,k}=\left(\mathbf{u}_{i+1,j,k}+\mathbf{u}_{i,j,k}\right)/2. \tag{51}$$

Taking the x-direction as an example, the corresponding interpolation stencil for WENO-5 is chosen as:

$$\mathbf{stencil}=\begin{cases}(i-2,j,k),(i-1,j,k),(i,j,k),(i+1,j,k),(i+2,j,k) & \text{if } \mathbf{u}_x\geq 0,\\ (i-1,j,k),(i,j,k),(i+1,j,k),(i+2,j,k),(i+3,j,k) & \text{if } \mathbf{u}_x<0.\end{cases} \tag{52}$$

Assuming that $\mathbf{u}_x\geq 0$ for instance, from Shu's work [65], we evaluate $\phi_{i+\frac{1}{2},j,k}$ in three different ways:

$$
\begin{aligned}
\phi^{(1)}_{i+\frac{1}{2},j,k}&=\frac{1}{3}\phi_{i-2,j,k}-\frac{7}{6}\phi_{i-1,j,k}+\frac{11}{6}\phi_{i,j,k},\\
\phi^{(2)}_{i+\frac{1}{2},j,k}&=-\frac{1}{6}\phi_{i-1,j,k}+\frac{5}{6}\phi_{i,j,k}+\frac{1}{3}\phi_{i+1,j,k},\\
\phi^{(3)}_{i+\frac{1}{2},j,k}&=\frac{1}{3}\phi_{i,j,k}+\frac{5}{6}\phi_{i+1,j,k}-\frac{1}{6}\phi_{i+2,j,k}.
\end{aligned}\tag{53}
$$

Similar to the 2D case, the final approximation is a convex combination of these three third-order approximations:

$$\phi_{i+\frac{1}{2},j,k}=\omega_1\phi^{(1)}_{i+\frac{1}{2},j,k}+\omega_2\phi^{(2)}_{i+\frac{1}{2},j,k}+\omega_3\phi^{(3)}_{i+\frac{1}{2},j,k}, \tag{54}$$

where the nonlinear weights ω_j of the WENO-5 scheme rely on the smoothness indicators β_j defined as:

$$\begin{aligned}
\beta_1 &= \frac{13}{12}\left(\phi_{i-2,j,k} - 2\phi_{i-1,j,k} + \phi_{i,j,k}\right)^2 \\
&\quad + \frac{1}{4}\left(\phi_{i-2,j,k} - 4\phi_{i-1,j,k} + 3\phi_{i,j,k}\right)^2, \\
\beta_2 &= \frac{13}{12}\left(\phi_{i-1,j,k} - 2\phi_{i,j,k} + \phi_{i+1,j,k}\right)^2 \\
&\quad + \frac{1}{4}\left(\phi_{i-1,j,k} - \phi_{i+1,j,k}\right)^{2,j,k}, \\
\beta_3 &= \frac{13}{12}\left(\phi_{i,j,k} - 2\phi_{i+1,j,k} + \phi_{i+2,j,k}\right)^2 \\
&\quad + \frac{1}{4}\left(3\phi_{i,j,k} - 4\phi_{i+1,j,k} + \phi_{i+2,j,k}\right)^2.
\end{aligned} \tag{55}$$

The nonlinear weights are computed as:

$$\omega_j = \frac{\tilde{\omega}_j}{\tilde{\omega}_1 + \tilde{\omega}_2 + \tilde{\omega}_3} \qquad \text{for } \tilde{\omega}_j = \frac{\gamma_j}{\left(\varepsilon + \beta_j\right)^2}, \tag{56}$$

where $\gamma_1 = \frac{1}{10}, \gamma_2 = \frac{3}{5}, \gamma_3 = \frac{3}{10}$, and ε is a small positive value set to 10^{-6} in our study. Calculations in other directions are similarly achieved.

A.3. Central-moment MRT models in D2Q9 and D3Q27 lattice structures

D2Q9 lattice structure: Based on [97], we define the shifted discrete lattice velocity as: $\overline{\mathbf{c}} = [\overline{\mathbf{c}}_x, \overline{\mathbf{c}}_y]$, where each term is written as $\overline{\mathbf{c}}_x = \mathbf{c}_x - \mathbf{u}_x$ and $\overline{\mathbf{c}}_y = \mathbf{c}_y - \mathbf{u}_y$, and $\mathbf{c}$ is one of the lattice velocities (see Appendix A.1 and Fig. 2). $\mathbf{u}$ is the local fluid velocity. Using the moment basis $[|T_0\rangle, \cdots, |T_8\rangle]$ defined as

$$\begin{aligned}
|\bar{T}_0\rangle &= \left||\mathbf{c}_i|^0\right\rangle,\ |\bar{T}_1\rangle = |\overline{c}_{xi}\rangle,\ |\bar{T}_2\rangle = |\overline{c}_{yi}\rangle, \\
|\bar{T}_3\rangle &= \left|\overline{c}_{xi}^2 + \overline{c}_{yi}^2\right\rangle,\ |\bar{T}_4\rangle = \left|\overline{c}_{xi}^2 - \overline{c}_{yi}^2\right\rangle, \\
|\bar{T}_5\rangle &= |\overline{c}_{xi}\overline{c}_{yi}\rangle,\ |\bar{T}_6\rangle = \left|\overline{c}_{xi}^2\overline{c}_{yi}\right\rangle, \\
|\bar{T}_7\rangle &= \left|\overline{c}_{xi}\overline{c}_{yi}^2\right\rangle,\ |\bar{T}_8\rangle = \left|\overline{c}_{xi}^2\overline{c}_{yi}^2\right\rangle,
\end{aligned} \tag{57}$$

the moment projection matrix $\mathbf{M}$ is expressed as

$$\mathbf{M} = \begin{bmatrix} \langle\bar{T}_0| \\ \langle\bar{T}_1| \\ \langle\bar{T}_2| \\ \langle\bar{T}_3| \\ \langle\bar{T}_4| \\ \langle\bar{T}_5| \\ \langle\bar{T}_6| \\ \langle\bar{T}_7| \\ \langle\bar{T}_8| \end{bmatrix} = \begin{bmatrix} |\mathbf{c}_0|^0 & |\mathbf{c}_1|^0 & \cdots & |\mathbf{c}_8|^0 \\ \overline{c}_{x,0} & \overline{c}_{x,1} & \cdots & \overline{c}_{x,8} \\ \overline{c}_{y,0} & \overline{c}_{y,1} & \cdots & \overline{c}_{y,8} \\ \overline{c}_{x,0}^2 + \overline{c}_{y,0}^2 & \overline{c}_{x,1}^2 + \overline{c}_{y,1}^2 & \cdots & \overline{c}_{x,8}^2 + \overline{c}_{y,8}^2 \\ \overline{c}_{x,0}^2 - \overline{c}_{y,0}^2 & \overline{c}_{x,1}^2 - \overline{c}_{y,1}^2 & \cdots & \overline{c}_{x,8}^2 - \overline{c}_{y,8}^2 \\ \overline{c}_{x,0}\overline{c}_{y,0} & \overline{c}_{x,1}\overline{c}_{y,1} & \cdots & \overline{c}_{x,8}\overline{c}_{y,8} \\ \overline{c}_{x,0}^2\overline{c}_{y,0} & \overline{c}_{x,1}^2\overline{c}_{y,1} & \cdots & \overline{c}_{x,8}^2\overline{c}_{y,8} \\ \overline{c}_{x,0}\overline{c}_{y,0}^2 & \overline{c}_{x,1}\overline{c}_{y,1}^2 & \cdots & \overline{c}_{x,8}\overline{c}_{y,8}^2 \\ \overline{c}_{x,0}^2\overline{c}_{y,0}^2 & \overline{c}_{x,1}^2\overline{c}_{y,1}^2 & \cdots & \overline{c}_{x,8}^2\overline{c}_{y,8}^2 \end{bmatrix}. \tag{58}$$

The relaxation matrix $\mathbf{S}$ in the moment space is a diagonal matrix, represented as $\mathbf{S} = \text{diag}[s_0, ..., s_i, ..., s_8]$. The relaxation rates s_i are related to the kinematic viscosity ν through:

$$s_i = \begin{cases} \left(\frac{\nu}{c_s^2} + \frac{1}{2}\right)^{-1} & \text{for } i \in \{4,5\}. \\ 1 \quad \text{otherwise}, \end{cases} \tag{59}$$

where ν can be computed using Eq. (11), while the total viscosity is $\nu \leftarrow \nu + \nu'$.

D3Q27 lattice structure: Similarly, the moment basis of D3Q27 is chosen as [15]:

$$\begin{aligned}
|\bar{T}_0\rangle &= \left||\mathbf{c}_i|^0\right\rangle,\ |\bar{T}_1\rangle = |\overline{c}_{xi}\rangle,\ |\bar{T}_2\rangle = |\overline{c}_{yi}\rangle,\ |\bar{T}_3\rangle = |\overline{c}_{zi}\rangle, \\
|\bar{T}_4\rangle &= |\overline{c}_{xi}\overline{c}_{yi}\rangle,\ |\bar{T}_5\rangle = |\overline{c}_{xi}\overline{c}_{zi}\rangle,\ |\bar{T}_6\rangle = |\overline{c}_{yi}\overline{c}_{zi}\rangle, \\
|\bar{T}_7\rangle &= \left|\overline{c}_{xi}^2 - \overline{c}_{yi}^2\right\rangle,\ |\bar{T}_8\rangle = \left|\overline{c}_{xi}^2 - \overline{c}_{zi}^2\right\rangle,
\end{aligned}$$

$$
\begin{aligned}
|\bar{T}_9\rangle &= \left|\bar{c}_{xi}^2+\bar{c}_{yi}^2+\bar{c}_{zi}^2\right\rangle,\ |\bar{T}_{10}\rangle = \left|\bar{c}_{xi}\bar{c}_{yi}^2+\bar{c}_{xi}\bar{c}_{zi}^2\right\rangle,\\
|\bar{T}_{11}\rangle &= \left|\bar{c}_{xi}^2\bar{c}_{yi}+\bar{c}_{yi}\bar{c}_{zi}^2\right\rangle,\ |\bar{T}_{12}\rangle = \left|\bar{c}_{xi}^2\bar{c}_{zi}+\bar{c}_{yi}^2\bar{c}_{zi}\right\rangle,\\
|\bar{T}_{13}\rangle &= \left|\bar{c}_{xi}\bar{c}_{yi}^2-\bar{c}_{xi}\bar{c}_{zi}^2\right\rangle,\ |\bar{T}_{14}\rangle = \left|\bar{c}_{xi}^2\bar{c}_{yi}-\bar{c}_{yi}\bar{c}_{zi}^2\right\rangle,\\
|\bar{T}_{15}\rangle &= \left|\bar{c}_{xi}^2\bar{c}_{zi}-\bar{c}_{yi}^2\bar{c}_{zi}\right\rangle,\ |\bar{T}_{16}\rangle = \left|\bar{c}_{xi}\bar{c}_{yi}\bar{c}_{zi}\right\rangle,\\
|\bar{T}_{17}\rangle &= \left|\bar{c}_{xi}^2\bar{c}_{yi}^2+\bar{c}_{xi}^2\bar{c}_{zi}^2+\bar{c}_{yi}^2\bar{c}_{zi}^2\right\rangle,\ |\bar{T}_{18}\rangle = \left|\bar{c}_{xi}^2\bar{c}_{yi}^2+\bar{c}_{xi}^2\bar{c}_{zi}^2-\bar{c}_{yi}^2\bar{c}_{zi}^2\right\rangle,\\
|\bar{T}_{19}\rangle &= \left|\bar{c}_{xi}^2\bar{c}_{yi}^2-\bar{c}_{xi}^2\bar{c}_{zi}^2\right\rangle,\ |\bar{T}_{20}\rangle = \left|\bar{c}_{xi}^2\bar{c}_{yi}\bar{c}_{zi}\right\rangle,\\
|\bar{T}_{21}\rangle &= \left|\bar{c}_{xi}\bar{c}_{yi}^2\bar{c}_{zi}\right\rangle,\ |\bar{T}_{22}\rangle = \left|\bar{c}_{xi}\bar{c}_{yi}\bar{c}_{zi}^2\right\rangle,\\
|\bar{T}_{23}\rangle &= \left|\bar{c}_{xi}\bar{c}_{yi}^2\bar{c}_{zi}^2\right\rangle,\ |\bar{T}_{24}\rangle = \left|\bar{c}_{xi}^2\bar{c}_{yi}\bar{c}_{zi}^2\right\rangle,\\
|\bar{T}_{25}\rangle &= \left|\bar{c}_{xi}^2\bar{c}_{yi}^2\bar{c}_{zi}\right\rangle,\ |\bar{T}_{26}\rangle = \left|\bar{c}_{xi}^2\bar{c}_{yi}^2\bar{c}_{zi}^2\right\rangle.
\end{aligned}
\tag{60}
$$

The shifted discrete lattice velocity with each component is: $\bar{\mathbf{c}} = [\bar{\mathbf{c}}_x, \bar{\mathbf{c}}_y, \bar{\mathbf{c}}_z]$, where each term is written as $\bar{\mathbf{c}}_x = \mathbf{c}_x - \mathbf{u}_x$, $\bar{\mathbf{c}}_y = \mathbf{c}_y - \mathbf{u}_y$ and $\bar{\mathbf{c}}_z = \mathbf{c}_z - \mathbf{u}_z$. The moment projection matrix $\mathbf{M}$ is expressed as

$$
\mathbf{M} = \begin{bmatrix} |\bar{T}_0\rangle \\ |\bar{T}_1\rangle \\ |\bar{T}_2\rangle \\ |\bar{T}_3\rangle \\ \vdots \\ |\bar{T}_{23}\rangle \\ |\bar{T}_{24}\rangle \\ |\bar{T}_{25}\rangle \\ |\bar{T}_{26}\rangle \end{bmatrix} = \begin{bmatrix} |\mathbf{c}_0|^0 & |\mathbf{c}_1|^0 & \cdots & |\mathbf{c}_{26}|^0 \\ \bar{c}_{x,0} & \bar{c}_{x,1} & \cdots & \bar{c}_{x,26} \\ \bar{c}_{y,0} & \bar{c}_{y,1} & \cdots & \bar{c}_{y,26} \\ \bar{c}_{z,0} & \bar{c}_{z,1} & \cdots & \bar{c}_{z,26} \\ \vdots & \vdots & \ddots & \vdots \\ \bar{c}_{x,0}\bar{c}_{y,0}^2\bar{c}_{z,0}^2 & \bar{c}_{x,1}\bar{c}_{y,1}^2\bar{c}_{z,1}^2 & \cdots & \bar{c}_{x,8}\bar{c}_{y,8}^2\bar{c}_{z,8}^2 \\ \bar{c}_{x,0}^2\bar{c}_{y,0}\bar{c}_{z,0}^2 & \bar{c}_{x,1}^2\bar{c}_{y,1}\bar{c}_{z,1}^2 & \cdots & \bar{c}_{x,8}^2\bar{c}_{y,8}\bar{c}_{z,8}^2 \\ \bar{c}_{x,0}^2\bar{c}_{y,0}^2\bar{c}_{z,0} & \bar{c}_{x,1}^2\bar{c}_{y,1}^2\bar{c}_{z,1} & \cdots & \bar{c}_{x,8}^2\bar{c}_{y,8}^2\bar{c}_{z,8} \\ \bar{c}_{x,0}^2\bar{c}_{y,0}^2\bar{c}_{z,0}^2 & \bar{c}_{x,1}^2\bar{c}_{y,1}^2\bar{c}_{z,1}^2 & \cdots & \bar{c}_{x,8}^2\bar{c}_{y,8}^2\bar{c}_{z,8}^2 \end{bmatrix}.
\tag{61}
$$

The relaxation rates s_i are defined as:

$$
s_i = \begin{cases} \left(\frac{\nu}{c_s^2}+\frac{1}{2}\right)^{-1} & \text{for } i \in \{4,5,6,7,8\}. \\ 1 & \text{otherwise,} \end{cases}
\tag{62}
$$

where ν can be computed using Eq. (11), while the total viscosity is $\nu \leftarrow \nu + \nu'$.

References

[1] T. Wacławczyk, On a relation between the volume of fluid, level-set and phase field interface models, Int. J. Multiph. Flow 97 (2017) 60–77.
[2] S. Mirjalili, S.S. Jain, M. Dodd, Interface-Capturing Methods for Two-Phase Flows: An Overview and Recent Developments, Center for Turbulence Research Annual Research Briefs, vol. 2017, 2017, pp. 117–135.
[3] A. Novick-Cohen, L.A. Segel, Nonlinear aspects of the Cahn-Hilliard equation, Physica D 10 (3) (1984) 277–298.
[4] T. Ilmanen, et al., Convergence of the Allen-Cahn equation to Brakke's motion by mean curvature, J. Differ. Geom. 38 (2) (1993) 417–461.
[5] D.M. Anderson, G.B. McFadden, A.A. Wheeler, Diffuse-interface methods in fluid mechanics, Annu. Rev. Fluid Mech. 30 (1) (1998) 139–165.
[6] D. Jacqmin, Calculation of two-phase Navier–Stokes flows using phase-field modeling, J. Comput. Phys. 155 (1) (1999) 96–127.
[7] A. Prosperetti, G. Tryggvason, Computational Methods for Multiphase Flow, Cambridge University Press, 2009.
[8] R. Eymard, T. Gallouët, R. Herbin, Finite volume methods, Handb. Numer. Anal. 7 (2000) 713–1018.
[9] S. Chen, G.D. Doolen, Lattice Boltzmann method for fluid flows, Annu. Rev. Fluid Mech. 30 (1) (1998) 329–364.
[10] C.E. Brennen, C.E. Brennen, Fundamentals of Multiphase Flow, Cambridge University Press, 2005.
[11] D. d'Humieres, Multiple–relaxation–time lattice Boltzmann models in three dimensions, Philos. Trans. R. Soc. Lond. Ser. A Math. Phys. Eng. Sci. 360 (1792) (2002) 437–451.
[12] D. D'Humières, I. Ginzburg, M. Krafczyk, P. Lallemand, L.-S. Luo, Multiple-relaxation-time lattice Boltzmann models in three dimensions, Philos. Trans. R. Soc. A: Math. Phys. Eng. Sci. 360 (1792) (2002) 437–451.
[13] M. Geier, A. Greiner, J.G. Korvink, Cascaded digital lattice Boltzmann automata for high Reynolds number flow, Phys. Rev. E 73 (6) (2006) 066705.
[14] M. Geier, A. Greiner, J.G. Korvink, A factorized central moment lattice Boltzmann method, Eur. Phys. J. Spec. Top. 171 (1) (2009) 55–61.
[15] A. De Rosis, Nonorthogonal central-moments-based lattice Boltzmann scheme in three dimensions, Phys. Rev. E 95 (1) (2017) 013310.
[16] C. Coreixas, G. Wissocq, G. Puigt, J.-F. Boussuge, P. Sagaut, Recursive regularization step for high-order lattice Boltzmann methods, Phys. Rev. E 96 (3) (2017) 033306.
[17] M. Geier, M. Schönherr, A. Pasquali, M. Krafczyk, The cumulant lattice Boltzmann equation in three dimensions: theory and validation, Comput. Math. Appl. 70 (4) (2015) 507–547.
[18] M. Geier, A. Pasquali, M. Schönherr, Parametrization of the cumulant lattice Boltzmann method for fourth order accurate diffusion Part I: derivation and validation, J. Comput. Phys. 348 (2017) 862–888.
[19] Y.P. Sitompul, T. Aoki, A filtered cumulant lattice Boltzmann method for violent two-phase flows, J. Comput. Phys. 390 (2019) 93–120.

[20] T. Zhang, B. Shi, Z. Guo, Z. Chai, J. Lu, General bounce-back scheme for concentration boundary condition in the lattice-Boltzmann method, Phys. Rev. E 85 (1) (2012) 016701.
[21] X. Yin, J. Zhang, An improved bounce-back scheme for complex boundary conditions in lattice Boltzmann method, J. Comput. Phys. 231 (11) (2012) 4295–4303.
[22] X. He, L.-S. Luo, Theory of the lattice Boltzmann method: from the Boltzmann equation to the lattice Boltzmann equation, Phys. Rev. E 56 (6) (1997) 6811.
[23] W. Li, Y. Chen, M. Desbrun, C. Zheng, X. Liu, Fast and scalable turbulent flow simulation with two-way coupling, ACM Trans. Graph. 39 (4) (2020) 47.
[24] E.H. Dowell, K.C. Hall, Modeling of fluid-structure interaction, Annu. Rev. Fluid Mech. 33 (1) (2001) 445–490.
[25] G. Trapani, R.M. Brionnaud, D.M. Holman, Non-linear fluid-structure interaction using a partitioned lattice Boltzmann-FEA approach, in: 46th AIAA Fluid Dynamics Conference, 2016, p. 3636.
[26] B.E. Griffith, N.A. Patankar, Immersed methods for fluid–structure interaction, Annu. Rev. Fluid Mech. 52 (2020) 421–448.
[27] A.K. Gunstensen, D.H. Rothman, S. Zaleski, G. Zanetti, Lattice Boltzmann model of immiscible fluids, Phys. Rev. A 43 (8) (1991) 4320–4327.
[28] D. Grunau, S. Chen, K. Eggert, A lattice Boltzmann model for multiphase fluid flows, Phys. Fluids A, Fluid Dyn. 5 (10) (1993) 2557–2562.
[29] S. Leclaire, M. Reggio, J.-Y. Trépanier, Isotropic color gradient for simulating very high-density ratios with a two-phase flow lattice Boltzmann model, Comput. Fluids 48 (1) (2011) 98–112.
[30] Y. Ba, H. Liu, Q. Li, Q. Kang, J. Sun, Multiple-relaxation-time color-gradient lattice Boltzmann model for simulating two-phase flows with high density ratio, Phys. Rev. E 94 (2) (2016) 023310.
[31] S. Saito, A. De Rosis, A. Festuccia, A. Kaneko, Y. Abe, K. Koyama, Color-gradient lattice Boltzmann model with nonorthogonal central moments: hydrodynamic melt-jet breakup simulations, Phys. Rev. E 98 (1) (2018) 013305.
[32] M.R. Swift, W. Osborn, J. Yeomans, Lattice Boltzmann simulation of nonideal fluids, Phys. Rev. Lett. 75 (5) (1995) 830–833.
[33] J. Shao, C. Shu, H. Huang, Y. Chew, Free-energy-based lattice Boltzmann model for the simulation of multiphase flows with density contrast, Phys. Rev. E 89 (3) (2014) 033309.
[34] X.-D. Niu, Y. Li, Y.-R. Ma, M.-F. Chen, X. Li, Q.-Z. Li, A mass-conserving multiphase lattice Boltzmann model for simulation of multiphase flows, Phys. Fluids 30 (1) (2018) 013302.
[35] E. Orlandini, M.R. Swift, J. Yeomans, A lattice Boltzmann model of binary-fluid mixtures, Europhys. Lett. 32 (6) (1995) 463.
[36] M.R. Swift, E. Orlandini, W. Osborn, J. Yeomans, Lattice Boltzmann simulations of liquid-gas and binary fluid systems, Phys. Rev. E 54 (5) (1996) 5041.
[37] D.J. Holdych, D. Rovas, J.G. Georgiadis, R.O. Buckius, An improved hydrodynamics formulation for multiphase flow lattice-Boltzmann models, Int. J. Mod. Phys. C 9 (08) (1998) 1393–1404.
[38] T. Inamuro, N. Konishi, F. Ogino, A Galilean invariant model of the lattice Boltzmann method for multiphase fluid flows using free-energy approach, Comput. Phys. Commun. 129 (1–3) (2000) 32–45.
[39] A.N. Kalarakis, V.N. Burganos, A.C. Payatakes, Galilean-invariant lattice-Boltzmann simulation of liquid-vapor interface dynamics, Phys. Rev. E 65 (5) (2002) 056702.
[40] H. Zheng, C. Shu, Y.-T. Chew, A lattice Boltzmann model for multiphase flows with large density ratio, J. Comput. Phys. 218 (1) (2006) 353–371.
[41] G. Falcucci, S. Ubertini, C. Biscarini, S. Di Francesco, D. Chiappini, S. Palpacelli, A. De Maio, S. Succi, Lattice Boltzmann methods for multiphase flow simulations across scales, Commun. Comput. Phys. 9 (2) (2011) 269–296.
[42] A. Fakhari, T. Mitchell, C. Leonardi, D. Bolster, Improved locality of the phase-field lattice-Boltzmann model for immiscible fluids at high density ratios, Phys. Rev. E 96 (5) (2017) 053301.
[43] P.-H. Chiu, Y.-T. Lin, A conservative phase field method for solving incompressible two-phase flows, J. Comput. Phys. 230 (1) (2011) 185–204.
[44] M. Geier, A. Fakhari, T. Lee, Conservative phase-field lattice Boltzmann model for interface tracking equation, Phys. Rev. E 91 (6) (2015) 063309.
[45] T. Mitchell, C. Leonardi, A. Fakhari, Development of a three-dimensional phase-field lattice Boltzmann method for the study of immiscible fluids at high density ratios, Int. J. Multiph. Flow 107 (2018) 1–15.
[46] H. Liang, J. Xu, J. Chen, H. Wang, Z. Chai, B. Shi, Phase-field-based lattice Boltzmann modeling of large-density-ratio two-phase flows, Phys. Rev. E 97 (3) (2018) 033309.
[47] F. Hajabdollahi, K.N. Premnath, S.W. Welch, Central moment lattice Boltzmann method using a pressure-based formulation for multiphase flows at high density ratios and including effects of surface tension and Marangoni stresses, J. Comput. Phys. 425 (2021) 109893.
[48] J. Latt, How to implement your DdQq dynamics with only q variables per node (instead of 2q), Tech. Rep., Tufts University, 2007.
[49] J. Shao, C. Shu, A hybrid phase field multiple relaxation time lattice Boltzmann method for the incompressible multiphase flow with large density contrast, Int. J. Numer. Methods Fluids 77 (9) (2015) 526–543.
[50] A. Zhang, J. Du, Z. Guo, Q. Wang, S. Xiong, Conservative phase-field method with a parallel and adaptive-mesh-refinement technique for interface tracking, Phys. Rev. E 100 (2) (2019) 023305.
[51] S.M. Allen, J.W. Cahn, Ground state structures in ordered binary alloys with second neighbor interactions, Acta Metall. 20 (3) (1972) 423–433.
[52] A. Fakhari, D. Bolster, L.-S. Luo, A weighted multiple-relaxation-time lattice Boltzmann method for multiphase flows and its application to partial coalescence cascades, J. Comput. Phys. 341 (2017) 22–43.
[53] C. Zhang, L.-P. Wang, H. Liang, Z. Guo, Central-moment discrete unified gas-kinetic scheme for incompressible two-phase flows with large density ratio, J. Comput. Phys. 482 (2023) 112040.
[54] Y. Sun, C. Beckermann, Sharp interface tracking using the phase-field equation, J. Comput. Phys. 220 (2) (2007) 626–653.
[55] V.M. Kendon, M.E. Cates, I. Pagonabarraga, J.-C. Desplat, P. Bladon, Inertial effects in three-dimensional spinodal decomposition of a symmetric binary fluid mixture: a lattice Boltzmann study, J. Fluid Mech. 440 (2001) 147–203.
[56] V.E. Badalassi, H.D. Ceniceros, S. Banerjee, Computation of multiphase systems with phase field models, J. Comput. Phys. 190 (2) (2003) 371–397.
[57] H.G. Lee, J. Kim, An efficient and accurate numerical algorithm for the vector-valued Allen–Cahn equations, Comput. Phys. Commun. 183 (10) (2012) 2107–2115.
[58] J. Shen, Modeling and numerical approximation of two-phase incompressible flows by a phase-field approach, in: Multiscale Modeling and Analysis for Materials Simulation, World Scientific, 2012, pp. 147–195.
[59] H. Liang, B. Shi, Z. Guo, Z. Chai, Phase-field-based multiple-relaxation-time lattice Boltzmann model for incompressible multiphase flows, Phys. Rev. E 89 (5) (2014) 053320.
[60] P. Constantin, C. Foias, Navier-Stokes Equations, University of Chicago Press, 1988.
[61] T. Lee, L. Liu, Lattice Boltzmann simulations of micron-scale drop impact on dry surfaces, J. Comput. Phys. 229 (20) (2010) 8045–8063.
[62] F. Ducros, F. Nicoud, T. Poinsot, Wall-adapting local eddy-viscosity models for simulations in complex geometries, Numer. Methods Fluid Dyn. VI (1998) 293–299.
[63] Z. Xie, T. Stoesser, A three-dimensional Cartesian cut-cell/volume-of-fluid method for two-phase flows with moving bodies, J. Comput. Phys. 416 (2020) 109536.
[64] A. Kumar, Isotropic finite-differences, J. Comput. Phys. 201 (1) (2004) 109–118.
[65] C.-W. Shu, High order weighted essentially nonoscillatory schemes for convection dominated problems, SIAM Rev. 51 (1) (2009) 82–126.
[66] G.-S. Jiang, C.-W. Shu, Efficient implementation of weighted eno schemes, J. Comput. Phys. 126 (1) (1996) 202–228.
[67] A. Fakhari, T. Mitchell, C. Leonardi, D. Bolster, Improved locality of the phase-field lattice-Boltzmann model for immiscible fluids at high density ratios, Phys. Rev. E 96 (5) (2017) 053301.
[68] L. Fei, K.H. Luo, Q. Li, Three-dimensional cascaded lattice Boltzmann method: improved implementation and consistent forcing scheme, Phys. Rev. E 97 (5) (2018) 053309.

[69] Y. Ning, K.N. Premnath, D.V. Patil, Numerical study of the properties of the central moment lattice Boltzmann method, Int. J. Numer. Methods Fluids 82 (2) (2016) 59–90.
[70] A. De Rosis, C. Coreixas, Multiphysics flow simulations using D3Q19 lattice Boltzmann methods based on central moments, Phys. Fluids 32 (11) (2020) 117101.
[71] A. De Rosis, R. Huang, C. Coreixas, Universal formulation of central-moments-based lattice Boltzmann method with external forcing for the simulation of multiphysics phenomena, Phys. Fluids 31 (11) (2019) 117102.
[72] D. Jacqmin, Contact-line dynamics of a diffuse fluid interface, J. Fluid Mech. 402 (2000) 57–88.
[73] A. Fakhari, D. Bolster, Diffuse interface modeling of three-phase contact line dynamics on curved boundaries: a lattice Boltzmann model for large density and viscosity ratios, J. Comput. Phys. 334 (2017) 620–638.
[74] Y. Chen, W. Li, R. Fan, X. Liu, Gpu optimization for high-quality kinetic fluid simulation, IEEE Trans. Vis. Comput. Graph. 28 (09) (2022) 3235–3251.
[75] A. De Rosis, E. Enan, A three-dimensional phase-field lattice Boltzmann method for incompressible two-components flows, Phys. Fluids 33 (4) (2021) 043315.
[76] C. Zhang, H. Liang, Z. Guo, L.-P. Wang, Discrete unified gas-kinetic scheme for the conservative Allen-Cahn equation, Phys. Rev. E 105 (4) (2022) 045317.
[77] Y. Zu, A. Li, H. Wei, Phase-field lattice Boltzmann model for interface tracking of a binary fluid system based on the Allen–Cahn equation, Phys. Rev. E 102 (5) (2020) 053307.
[78] Y. Zu, S. He, Phase-field-based lattice Boltzmann model for incompressible binary fluid systems with density and viscosity contrasts, Phys. Rev. E 87 (4) (2013) 043301.
[79] H. Wang, Z. Chai, B. Shi, H. Liang, Comparative study of the lattice Boltzmann models for Allen-Cahn and Cahn-Hilliard equations, Phys. Rev. E 94 (3) (2016) 033304.
[80] Z. Yang, C. Zhong, C. Zhuo, et al., Phase-field method based on discrete unified gas-kinetic scheme for large-density-ratio two-phase flows, Phys. Rev. E 99 (4) (2019) 043302.
[81] H. Ding, P.D. Spelt, C. Shu, Diffuse interface model for incompressible two-phase flows with large density ratios, J. Comput. Phys. 226 (2) (2007) 2078–2095.
[82] F. Ren, B. Song, M.C. Sukop, H. Hu, Improved lattice Boltzmann modeling of binary flow based on the conservative Allen-Cahn equation, Phys. Rev. E 94 (2) (2016) 023311.
[83] E. Dinesh Kumar, S. Sannasiraj, V. Sundar, Phase field lattice Boltzmann model for air-water two phase flows, Phys. Fluids 31 (7) (2019) 072103.
[84] X. He, S. Chen, R. Zhang, A lattice Boltzmann scheme for incompressible multiphase flow and its application in simulation of Rayleigh–Taylor instability, J. Comput. Phys. 152 (2) (1999) 642–663.
[85] S.A. Hosseini, H. Safari, D. Thevenin, Lattice Boltzmann solver for multiphase flows: application to high Weber and Reynolds numbers, Entropy 23 (2) (2021) 166.
[86] X. He, R. Zhang, S. Chen, G.D. Doolen, On the three-dimensional Rayleigh–Taylor instability, Phys. Fluids 11 (5) (1999) 1143–1152.
[87] S. Saito, Y. Abe, K. Koyama, Lattice Boltzmann modeling and simulation of liquid jet breakup, Phys. Rev. E 96 (1) (2017) 013317.
[88] H.G. Lee, J. Kim, Numerical simulation of the three-dimensional Rayleigh–Taylor instability, Comput. Math. Appl. 66 (8) (2013) 1466–1474.
[89] D. Bhaga, M. Weber, Bubbles in viscous liquids: shapes, wakes and velocities, J. Fluid Mech. 105 (1981) 61–85.
[90] R. Clift, J.R. Grace, M.E. Weber, Bubbles, Drops, and Particles, Courier Corporation, 2005.
[91] S. Hysing, S. Turek, D. Kuzmin, N. Parolini, E. Burman, S. Ganesan, L. Tobiska, Proposal for Quantitative Benchmark Computations of Bubble Dynamics, 2007.
[92] S. Aland, A. Voigt, Benchmark computations of diffuse interface models for two-dimensional bubble dynamics, Int. J. Numer. Methods Fluids 69 (3) (2012) 747–761.
[93] S. Hysing, S. Turek, D. Kuzmin, N. Parolini, E. Burman, S. Ganesan, L. Tobiska, Quantitative benchmark computations of two-dimensional bubble dynamics, Int. J. Numer. Methods Fluids 60 (11) (2009) 1259–1288.
[94] X. Chen, S. Mandre, J.J. Feng, Partial coalescence between a drop and a liquid-liquid interface, Phys. Fluids 18 (5) (2006) 051705.
[95] M.M. Kamra, J. Al Salami, M. Sueyoshi, C. Hu, Experimental study of the interaction of dambreak with a vertical cylinder, J. Fluids Struct. 86 (2019) 185–199.
[96] C. Ma, J. Wu, T. Zhang, A high order spectral difference-based phase field lattice Boltzmann method for incompressible two-phase flows, Phys. Fluids 32 (12) (2020).
[97] A. De Rosis, Non-orthogonal central moments relaxing to a discrete equilibrium: a D2Q9 lattice Boltzmann model, Europhys. Lett. 116 (4) (2017) 44003.